



HAL
open science

Elemental and isotopic compositions of trench-slope black shales, Bohemian Massif, with implications for oceanic and atmospheric oxygenation in early Cambrian

Jan Pašava, Lukáš Ackerman, Jiří Žák, František Veselovský, Robert A Creaser, Martin Svojtka, Béatrice Luais, Ondřej Pour, Ondřej Šebek, Jakub Trubač, et al.

► To cite this version:

Jan Pašava, Lukáš Ackerman, Jiří Žák, František Veselovský, Robert A Creaser, et al.. Elemental and isotopic compositions of trench-slope black shales, Bohemian Massif, with implications for oceanic and atmospheric oxygenation in early Cambrian. *Palaeogeography, Palaeoclimatology, Palaeoecology*, 2021, 564, pp.110195. 10.1016/j.palaeo.2020.110195 . hal-03442502

HAL Id: hal-03442502

<https://hal.univ-lorraine.fr/hal-03442502>

Submitted on 23 Nov 2021

HAL is a multi-disciplinary open access archive for the deposit and dissemination of scientific research documents, whether they are published or not. The documents may come from teaching and research institutions in France or abroad, or from public or private research centers.

L'archive ouverte pluridisciplinaire **HAL**, est destinée au dépôt et à la diffusion de documents scientifiques de niveau recherche, publiés ou non, émanant des établissements d'enseignement et de recherche français ou étrangers, des laboratoires publics ou privés.

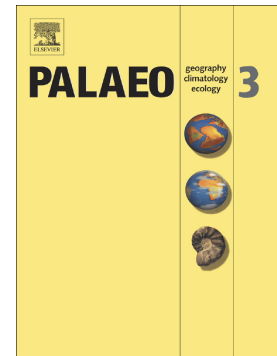


Distributed under a Creative Commons Attribution - NonCommercial - NoDerivatives 4.0 International License

Journal Pre-proof

Elemental and isotopic compositions of trench-slope black shales, Bohemian Massif, with implications for oceanic and atmospheric oxygenation in early Cambrian

Jan Pašava, Lukáš Ackerman, Jiří Žák, František Veselovský, Robert A. Creaser, Martin Svojtka, Béatrice Luais, Ondřej Pour, Ondřej Šebek, Jakub Trubač, Eva Vosáhllová, Damien Cividini



PII: S0031-0182(20)30643-X

DOI: <https://doi.org/10.1016/j.palaeo.2020.110195>

Reference: PALAEO 110195

To appear in: *Palaeogeography, Palaeoclimatology, Palaeoecology*

Received date: 8 September 2020

Revised date: 18 December 2020

Accepted date: 21 December 2020

Please cite this article as: J. Pašava, L. Ackerman, J. Žák, et al., Elemental and isotopic compositions of trench-slope black shales, Bohemian Massif, with implications for oceanic and atmospheric oxygenation in early Cambrian, *Palaeogeography, Palaeoclimatology, Palaeoecology* (2018), <https://doi.org/10.1016/j.palaeo.2020.110195>

This is a PDF file of an article that has undergone enhancements after acceptance, such as the addition of a cover page and metadata, and formatting for readability, but it is not yet the definitive version of record. This version will undergo additional copyediting, typesetting and review before it is published in its final form, but we are providing this version to give early visibility of the article. Please note that, during the production process, errors may be discovered which could affect the content, and all legal disclaimers that apply to the journal pertain.

Elemental and isotopic compositions of trench-slope black shales, Bohemian Massif, with implications for oceanic and atmospheric oxygenation in early Cambrian

Jan Pašava^{a,*}, Lukáš Ackerman^{a,b}, Jiří Žák^c, František Veselovský^a, Robert A. Creaser^d, Martin Svojtka^b, Béatrice Luais^e, Ondřej Pour^a, Ondřej Šebek^a, Jakub Trubač^c, Eva Vosáhllová^b, Damien Cividini^e

^a *Czech Geological Survey, Klárov 3, CZ-118 21 Prague 1, Czech Republic*

^b *Institute of Geology of the Czech Academy of Sciences, Rozvojová 269, CZ-165 00 Prague 6, Czech Republic*

^c *Institute of Geology and Paleontology, Faculty of Science, Charles University, Albertov 6, Prague, CZ-128 43, Czech Republic*

^d *Department of Earth and Atmospheric Sciences, Faculty of Science, University of Alberta, Edmonton, Canada*

^e *CRPG-CNRS, UMR 7558, Université de Lorraine, Nancy, France*

E-mail addresses: jan.pasava@geology.cz (corresponding author*), ackerman@gli.cas.cz, jirizak@natur.cuni.cz, frantisek.veselovsky@geology.cz, rcreaser@ualberta.ca, svojtka@gli.cas.cz, luais@crpg.cnrs-nancy.fr, ondrej.pour@geology.cz, ondrej.sebek@geology.cz, jakub.trubac@natur.cuni.cz, vosahlova@gli.cas.cz, cividini@crpg.cnrs-nancy.fr

Keywords: black shale, molybdenum, chromium, pyrite, LA ICP MS, geochronology

Abstract

This study examines a lower Cambrian pyrite-bearing black shale–graywacke succession in the Czech Republic interpreted as infill of a deep-marine, extensional trench-slope basin on top of an accretionary wedge that developed during subduction of an oceanic plate beneath the northern margin of Gondwana. The new U–Pb detrital zircon geochronology of the graywacke constrains the maximum age of deposition to 533 ± 6 Ma, whereas the Re–Os dating of pyrite yielded a younger age of 507 ± 16 Ma. Distribution of major and trace elements and calculated enrichment factors (EF) indicate that this succession was deposited under changing redox conditions over a short time span and that the basin was presumably controlled by tectonic subsidence and varying supply of terrigenous arc-derived material. This depositional setting is reflected by largely variable EFs and $\delta^{98}\text{Mo}$ and $\delta^{53}\text{Cr}$ values. Euxinic conditions detected at the base of the sampled black shale interval are documented by the highest values of EFs of redox-sensitive metals (e.g., Mo, U, V, Ni, Co, As) and also the C_{org}/P (>1000) and DOP_T (>0.7) values. Black shales show lower $\delta^{56}\text{Fe}$ values due to the excess of authigenic pyrite-Fe with a mean $\delta^{56}\text{Fe}$ value of -0.02 ‰ over detrital Fe in graywacke with a mean $\delta^{56}\text{Fe}$ value of $+0.25$ ‰. However, the Fe isotopic signatures of the black shales are not consistent with iron shuttling, mixing of authigenic and detrital sources, or hydrothermal metal enrichment. Instead, they most likely resulted from partial oxidation of pyrite through the syndepositional oxidizing hydrothermal fluids (Si–Ba enrichment), which resulted in precipitation of isotopically heavy Fe-oxyhydroxides. We propose that our maximal recorded $\delta^{98}\text{Mo}$ value ($+0.98$ ‰) might represent the best estimate for the ancient local seawater Mo composition at around 533 Ma and argues against deep-ocean oxygenation

in the early Cambrian. On the other hand, the Se/Co ratios of syngenetic pyrite indicate a mean atmosphere O₂ value of ~27 %.

1. Introduction

The Precambrian–Cambrian transition is marked by several major events that significantly reshaped the Earth’s surface environment. The breakup of the supercontinent Rodinia and the subsequent amalgamation of Gondwana (e.g., Li et al., 2008 and references therein), several major glaciations, including possible ‘Snowball’ Earth (e.g., Fairchild and Kennedy, 2007; Hoffman et al., 1998), and unprecedented biological innovations leading to the emergence of metazoans (e.g., Marshall, 2006; Narbonne, 2005), altogether mark a major turning point in the Earth’s history. This period is also known for a widespread (but not universal) oxygenation of the deep ocean (e.g., Canfield et al., 2007; Fike et al., 2006), which might have triggered the evolutionary innovations exemplified by the Ediacara Biota and Cambrian Explosion (e.g., Narbonne, 2005; Zhang et al., 2014 and references therein). Peters and Gaines (2012) suggested that early Paleozoic (540–480 Ma) marine sediments are indicative of increased oceanic alkalinity and enhanced chemical weathering of continental crust, which may have been an environmental trigger for the evolution of biomineralization and the Cambrian Explosion.

Black shales, which were deposited from the Archean to the present in different geotectonic settings (e.g., Arthur and Sageman, 1994 and references therein), represent a particularly informative archive of temporal variations in the chemical and isotopic (e.g., $\delta^{98}\text{Mo}$, $\delta^{53}\text{Cr}$, $\delta^{56}\text{Fe}$) composition of seawater (e.g., Ackerman et al., 2019a; Anbar et al., 2007; Dauphas et al., 2017; Kendall et al., 2017; Kurzweil et al., 2015; Siebert et al., 2005; Wille et al., 2013). They usually show a significant enrichment in metals (e.g., Mo, U, Fe, Cr, Ni, Cu, Zn) whose isotopic compositions are sensitive to changes in the seawater O₂ levels

and biological processes (Archer and Vance, 2008; Little et al., 2015, 2014; Moynier et al., 2017; Vance et al., 2017). Furthermore, elemental and isotopic ($\delta^{98}\text{Mo}$, $\delta^{56}\text{Fe}$, and $\delta^{53}\text{Cr}$) compositions of multiple sinks and sources were key for the cycling and mass balance of Mo, Fe, and Cr in the ocean through the Earth's history (e.g., Dauphas et al., 2017; Kendall et al., 2017; Qin and Wang, 2017).

The Paleoproterozoic Great Oxidation Event (2.4–2.3 Ga) and the Neoproterozoic Oxidation Event (0.8–0.5 Ga) resulted in change of the Earth's atmosphere and hydrosphere from an Archean anoxic to a modern oxygenated world (Och and Shields-Zhou, 2012 and references therein). Despite of numerous paleontologically- and geochemically-oriented studies employing a large number of proxies (e.g., redox sensitive elements and isotopes of S, Mo, Se, U, Cr) in marine pyritic black shales, levels of O_2 in the Precambrian and Phanerozoic atmosphere remain an important issue to be solved (see Large et al., 2019 for a detailed summary). A newly emerging and promising approach is the laser-ablation inductively coupled mass spectrometry (LA-ICP-MS), which has been increasingly used to analyze the redox-sensitive elements in pyrite in marine black shales (e.g., Berner et al., 2013; Large et al., 2019, 2014; Steadman et al., 2020 and references therein).

In order to improve our knowledge on the elemental and isotopic Mo, Cr, and Fe cycling and mass balance in the deep ocean and the pathways of their possible isotopic fractionation, we present new elemental and Mo, Cr, and Fe isotopic data for a superbly exposed early Cambrian black shale succession, referred to as the Liblín section, in the central part of the Bohemian Massif. The elemental and isotopic data are complemented with the Re–Os, sulfur isotope data and trace element composition of pyrite and with U–Pb geochronology on detrital zircon to constrain the maximum depositional age of the sedimentary succession. A new model is proposed to explain deposition of black shales on top of accretionary wedges and the

data are discussed with possible implications to the extent of Earth's surface and ocean oxygenation during the Cambrian Period.

2. Geological setting

The Bohemian Massif, the northeasternmost and the largest remnant of Late Paleozoic Variscan orogenic belt in Europe, is composed of several lithospheric units characterized by different tectonometamorphic evolution (Fig. 1; see, e.g., Franke, 2006, 2000; Schulmann et al., 2009 for overviews). The Teplá–Barrandian Unit (TBU) occupies the centre of the massif (Fig. 1c) and differs from the neighboring units by generally very low metamorphic grade and lack of pervasive (ductile) Variscan deformation except high-strain domains along its margins (e.g., Hajná et al., 2012; Peřestý et al., 2020, 2017). Consequently, the interior of the unit superbly preserves the pre-Variscan, Neoproterozoic (Cadomian) and Lower Paleozoic volcano-sedimentary successions.

The Cadomian basement is largely represented by the >600–527 Ma Blovice accretionary complex (BAC), underlying much of the Teplá–Barrandian Unit, and an inboard ~610–560 Ma volcanic arc (the Davle volcanic complex; Fig. 1d) overlain by the ~580–560 Ma Lečice black shales (Ackerman et al., 2021). The BAC developed during subduction of an oceanic plate beneath the northern margin of Gondwana and thus represents a part of the once extensive Avalonian–Cadomian belt (Fig. 1a, b; e.g., Ackerman et al., 2019b; Hajná et al., 2019, 2018, 2017; Linnemann et al., 2014; Nance et al., 2010, 1991; Žák et al., 2020). The internal architecture of the accretionary complex is defined by six fault-bounded belts, where three, mostly coherent, domains of arc-derived and multiply recycled deep-marine siliciclastic rocks (Belts I–III; Fig. 1d) alternate with belts of ocean-floor-bearing (ophiolitic) mélanges (Belts 1–3; Hajná et al., 2013; Fig. 1d). The former is represented by bedded siltstones, slates,

graywackes and (black) shales accompanied by cherts while the latter is characterized by block-and-matrix fabric, defined by basaltic blocks of tholeiitic and alkaline composition that are embedded in the siliciclastic matrix (Ackerman et al., 2019b; Pin and Waldhausrová, 2007). Recent geochronological data suggest that the individual belts within the Blovice accretionary complex are progressively younger to the northwest and that a large portion of the complex was accreted during early Cambrian until ~527 Ma (Žák et al., 2020). The upper age bracket for the accretionary processes is provided by granite to trondhjemite plutons that intrude the complex at ~524–522 Ma (Dörr et al., 2002, 1998).

The black shales, mined in the past for the production of the 'Bohemian' sulfuric acid (Pašava, 2000; Pašava et al., 2019, 1996), occur especially within the ophiolitic mélangé belts. They form concordant layers (horizons) within the graywacke successions, parallel to bedding (where preserved) and/or tectonic foliation (cleavage). The black shale horizons are several meters to several tens of meters thick and are strongly deformed due to their low competence relative to the host graywackes. In some places, the black shales enclose graywacke clasts and, vice versa, are found as angular to subangular clasts within graywackes (Hajná et al., 2013).

3. The Liblín section

3.1. Field relationships

The sampled Liblín section (adit - 49°55'11.5"N, 13°32'21.6"E, about 25 km NNE of Plzeň/Pilsen) is located ~500 m southeast from the tectonic boundary of the ophiolitic mélangé Belt 2 and overlying Belt II (the Radnice–Kralupy and Kralovice–Rakovník belts) in a structurally complex zone of superposed Variscan and Cadomian deformations (Figs. 1d, 2a). The boundary between both belts trends NE–SW and was recently mapped as a NW-dipping reverse fault, presumably formed during Variscan (Late Devonian to early

Carboniferous) compression (Fig. 2a). The sampled Liblín section occupies the footwall, composed of low-grade (prehnite-pumpellyite facies) monotonous succession of thinly bedded graywackes rhythmically alternating with slates and siltstones (Fig. 2b, c), altogether interpreted as deep-water turbidites (Cháb and Pelc, 1968). The belt also contains basalt blocks, several hundred meters across that are enclosed in a graywacke matrix with abundant slump structures (Fig. 2a). In contrast, the overlaying Belt 2 is dominated by thickly bedded to massive graywackes devoid of basalt blocks and slump structures. In a domain along the fault, relic bedding and tectonic cleavage in the graywacke–shale successions dip to the NW at moderate angles (Fig. 2a, b).

The sampled Liblín section represents a ~200-m-long NW–SSE-oriented outcrop predominantly formed as a result of the 18th century mining work focused on the pyrite-bearing black shales (Fig. 2b). Overall, the sedimentary package dips 30–50° to the NW and, from bottom to top, consists of three main units (Fig. 2b, c):

(1) The base of the section comprises alternating graywackes (bed thickness varies from 3–5 cm to several decimeters) and gray shales/siltstones, boudinaged and folded into decimeter-scale folds in some places. Quartz veins are particularly abundant, both discordant and parallel to the relic bedding. Massive graywacke was sampled for the U–Pb dating (LIB-ŠT-2) near the entrance to the main adit at a higher structural level of the section. Five samples (LIB-ŠT-3 to 7) were then collected from the overlaying graywacke–siltstone–shale lithology, spaced about 1.5 m apart (Fig. 2b).

(2) The section passes upwards into the main, approximately 30–40 m thick horizon of laminated black shales. This black shale exposure was sampled in detail with eleven collected samples (LIB-1/11; from bottom to top including sample P-LIB-ŠT-3 from the top of this section for Re–Os geochronology on pyrite; Fig. 2b) with spacing about 5 to 10 centimeters. The contact between underlying unit and the black shale horizon is marked by a ~3 m thick

reverse fault/shear zone (Fig. 2b) associated with pervasive fluid alteration. The alteration is expressed by the common presence of quartz veins and lenses and layers of Fe-hydroxides. The black shale horizon continues through the adit to an abandoned quarry for about 25 m, where pyrites for the Re–Os geochronology and *in-situ* trace element analyses were examined in the samples P-LIB-1/5 and 7, collected ~2 m below the contact with overlying unit (Fig. 2b).

(3) The uppermost unit of the section is thrust over the black shale horizon and is composed of siltstone/shale at the base, gradually passing to massive and bedded graywackes (Fig. 2b, c). Unlike the underlying units, the graywackes contain abundant black shale clasts, typically 3–5 mm in size.

3.2. Representative samples and petrography

Petrography of the representative samples of the units described above were examined in detail using polarized and reflected microscopy.

The graywacke (LIB-ŠT-2) is composed from the fine-grained matrix of plagioclase (commonly sericitized and chloritized) and quartz (~10–40 µm in size) accompanied by isolated larger grains (up to 0.5 mm) represented predominantly by quartz ± feldspar commonly showing irregular, dissolved margins (Fig. 3a). The matrix is cross-cut by abundant thin (< 100 µm) veins of microcrystalline quartz. In comparison, sample LIB-ŠT-6 is a laminated shale with fine-grained (~10–30 µm in size) plagioclase and quartz matrix composed of alternating bands some of which contain higher amounts of organic matter. The widespread silicification is expressed by the microcrystalline quartz that is disseminated throughout the matrix and by a network of irregular patches and veinlets (both parallel and discordant to lamination) with of microcrystalline quartz (Fig. 3b).

The LIB-1/11 is a fine-grained, laminated black shale rich in organic matter showing high degree of silicification expressed by large amounts of quartz disseminated in the matrix, microcrystalline quartz aggregates and veinlets both subparallel and discordant to the lamination (the latter are thin, < 60 μm ; Fig. 3c). The black shale contains abundant pyrite predominantly forming larger (up to 200 μm in size) grains intimately connected with quartz veinlets and rare, commonly framboidal and small (<20 μm) grains dispersed in Si- and organic matter-rich matrix. Sample LIB-1/6 is also organic-rich black shale with a similar texture to LIB-1/11, but differs in a smaller proportion of pyrite. Finally, the sample LIB-1/1 has texture similar to the graywacke described above with fine grained matrix accompanied by larger, irregular and commonly resorbed quartz grains. However, it differs in a much higher content of organic matter, expressed as abundant elongated patches dispersed within the matrix, and in the presence of large pyrite grains bound to diagenetic quartz veinlets.

Pyrite-rich black shales contain two textural types of pyrite (Fig. 3d). **Type I** is represented by syndepositional/early diagenetic pyrite forming framboidal as well as irregular small (mostly <20 μm) grains and microcrystals, locally forming stratiform layers in organic matter-rich silicified matrix. Locally, it is associated with barite grains in silicified matrix (Fig. 3e) and may contain microinclusions of sphalerite and chalcopyrite. It is accompanied by REE-phosphates (monazite, xenotime). **Type II** pyrite forms larger (up to ~400 μm) recrystallized grains and grainy aggregates associated with a widespread silicification in patches and bands sub-parallel as well discordant to the black shale lamination (Fig. 3d,f). Locally, it is altered to Fe-oxyhydroxide (Fig. 3g) and accompanied by grains of REE-phosphates (monazite, xenotime), apatite, albite, biotite and rutile dispersed in the rock matrix. This pyrite can also rarely contain micro-inclusions (Fig. 3h) of sphalerite, chalcopyrite, pyrrhotite and titanite and locally, it is intimately associated with grainy aggregate of molybdenite (not shown).

4. Analytical methods

Major element compositions were determined using a wet-chemistry (see Dempírová et al., 2010) at the Czech Geological Survey with the precision better than 5 %, whereas the accuracy, which was monitored by the long-term reproducibility of selected reference materials (e.g., JGB-3), was better than 10 % for all the analyzed oxides. Trace element contents were measured using an ICP-MS technique using Thermo *iCAP-Q* instrument at the Faculty of Science, Charles University, following the methods summarized in Strnad et al. (2005). The in-run precision was always better than 5 % (F.S.D.) and the accuracy based on the analyses of SBC-1 and SGR-1b certified reference materials (USGS) was better than 12 % for all analyzed elements.

Zircon U–Pb geochronology of underlying grey wacke (LIB-007) was carried out using *Element 2* ICP–MS (Thermo) coupled with a 213 nm NdYAG UP-213 laser ablation system (New Wave Research) at the Institute of Geology of the Czech Academy of Sciences using the procedures outlined in Haluzová et al. (2015). Elemental fractionation and instrumental mass bias were corrected by normalization of internal U–Pb calibration zircon standards 91500 and GJ-1 periodically analyzed during the measurement for quality control purposes. The obtained concordia ages of these standards 1065 ± 2 Ma (2σ) and 607 ± 1 Ma (2σ) correspond well within the errors to published zircon standards ages. Raw data reduction and age calculations, including corrections for baseline, instrumental drift, mass bias and down-hole fractionation, were carried out using the computer program Iolite (v. 3.0; Paton et al., 2011).

Pyrite separates were prepared by a combination of crushing, hand picking and leaching resulting in more than 95 % purity of the separates. Re–Os geochronology of the pyrite was carried out at the University of Alberta using protocols described in detail elsewhere (e.g.,

Morelli et al., 2010). The method includes decomposition in a concentrated HCl–HNO₃ mixture in Carius Tubes with the presence of ¹⁸⁵Re–¹⁹⁰Os spike and Re and Os separation by ion exchange chromatography and solvent extraction, respectively. Both Re and Os fractions were analyzed for their isotopic compositions using negative thermal ionization mass spectrometry (N-TIMS).

Stable isotopic composition of sulfur in pyrite was measured at Laboratory for Stable and Radiogenic Isotopes (Faculty of Science, Charles University, Prague), using Thermo *Flash 2000* elemental analyzer connected to a Thermo *Delta V Advantage* isotope ratio mass spectrometer in a Continuous Flow IV system. Minimal weight of samples depends on the wt. % amount of sulfur corresponding to a minimum of ~60 µg sulfur in the measured analyte. Samples wrapped in tin capsules were combusted with addition of V₂O₅ to boost the process (Yanagisawa and Sakai, 1983). Released gas (CO₂) was separated in a gas chromatography column and then transferred to mass spectrometer. The obtained δ³⁴S values are expressed relative to Vienna Canyon Diablo Troilite (V-CDT) using a calibration curve based on the measurements of international standards IAEA-S-3 (δ³⁴S = -32.2 ± 0.5 ‰; n = 7), IAEA-SO-5 (δ³⁴S = +0.5 ± 0.1 ‰; n = 9) and IAEA-SO-6 (δ³⁴S = -34.4 ± 0.2 ‰; n = 9).

Chromium isotopic analyses were acquired at the Czech Geological Survey. After dry ashing at 650 °C overnight, the samples were decomposed in a mixture of concentrated HNO₃, HCl, HF and H₂O₂ using a Mars microwave digestion system for several hours. Afterwards, the solutions were dried down doped with ⁵⁰Cr–⁵⁴Cr double-spike tracer and processed through ion-exchange column chemistry using the methods outlined in detail in Farkaš et al. (2013). Isotopic analyses were carried out by a MC–ICP–MS (*Neptune*, Thermo) coupled to a desolvating nebulizer system (Aridus II) and operated in high-resolution mode (see Farkaš et al., 2013 for details on mass spectrometry and data reduction). The δ⁵³Cr results (‰) were related to the NIST SRM 979. Accuracy of the measurement was evaluated using

USGS BHVO-2 (basalt) and SDO-1 (shale) reference materials yielding $\delta^{53}\text{Cr}$ of -0.11 ± 0.04 ‰ and -0.10 ± 0.04 ‰, respectively, in good agreement with the published GEOREM database values. The internal and external reproducibilities were controlled by measurement of sample replicates and yield ± 0.05 ‰.

Molybdenum isotopic composition was determined in the joint laboratory of the Institute of Geology of the Czech Academy of Sciences (chemistry) and the Czech Geological Survey (mass spectrometry), using the double-spike and MC-ICP-MS techniques outlined in detail in Gaspers et al. (2020). In brief, after ashing (see above), the sample powder was weighted along with ^{97}Mo – ^{100}Mo double spike and dissolved in a mixture of HF and HNO_3 at 140°C for 72 hours. Subsequently, the samples were processed through the ion-exchange chromatography using the guidelines of Willbold et al. (2015). Molybdenum isotopic analysis was carried out using a *Neptune* MC-ICP-MS (Thermo) using the methods outlined in detail in Gaspers et al. (2020). Isotopic compositions of Mo are reported as $\delta^{98}\text{Mo}$ against NIST 3134 standard solution. Total combined uncertainty (2SD) for the whole protocol was 0.06 ‰ as demonstrated on a long-term reproducibility of $\delta^{98}\text{Mo}$ values on NIST 3134 Mo solution and periodic analyses of several reference sedimentary materials – e.g., SGR-1b and SBC-1 yielding $+0.44 \pm 0.06$ ‰ and $+0.56 \pm 0.08$ ‰ (see Gaspers et al., 2020 for more data).

The iron isotopic compositions were performed at CRPG-Nancy, France using the purification outlined in Roskosz et al. (2006) and Marin-Carbonne et al. (2011). About 30 mg of sample powder was digested in a mixture of concentrated HF and HNO_3 in closed Savillex beakers on a hot plate at $\sim 90^\circ\text{C}$. This was followed by fluoride breakdown using multiple cycles of HNO_3 addition and the final residue was dissolved in 7 M HCl. Iron isolation was performed using AG-MP1 resin exchange chromatography (100–200 mesh) and ~ 50 μg Fe in the loaded solution. Afterwards, Fe fraction was eluted with 2 M HCl, dried down and finally converted to nitride using 7 M HNO_3 . Dry Fe residues were further dissolved in 0.05 M

HNO₃ for isotopic measurements carried out using the *Neptune Plus* MC–ICP–MS housed at CRPG Nancy, and following the procedures detailed in Marin-Carbonne et al. (2011), Liu et al. (2014), and El Korh et al. (2017). The instrument was operated in high-resolution mode ($M/\Delta M \approx 9000$) allowing resolving argide interferences on Fe masses while ⁵⁴Cr interference on ⁵⁴Fe was corrected by monitoring ⁵³Cr and using a ⁵⁴Cr/⁵³Cr ratio of 0.248921 (Rosman and Taylor, 1998). The iron isotopic measurement follows the sample/standard bracketing method using IRMM-014 standard solution and the data are expressed as $\delta^{56}\text{Fe}$ with a long-term external reproducibility (2SD) better than 0.08‰ on average. Accuracy of the whole protocol was evaluated by replicate analyses of IF-G (banded iron formation, CRPG) and BIR-1 (basalt, USGS) reference materials yielding $\delta^{56}\text{Fe}$ on $+0.65 \pm 0.13 \text{ ‰}$ and $+0.10 \pm 0.03 \text{ ‰}$, respectively, in agreement with previous studies (e.g., Craddock and Dauphas, 2011).

The polished sections with two types of pyrite grains were first studied using a reflected light microscopy and afterwards by a FE–SEM scanning microscopy using Tescan Mira3 GMU housed at the Czech Geological Survey. Subsequently, two generations of pyrites were selected for *in-situ* trace element analyses: (1) fine-grain pyrite crystals and framboids and (2) coarse grained pyrite grains; both have been analyzed by an *Element 2* sector-field ICP–MS coupled with a 213 nm NYAG UP-213 laser ablation system (New Wave Research) housed at the Institute of Geology of the Czech Academy of Sciences. Samples were analyzed at the repetition rate of 20 Hz, the laser fluence of 3 J/cm² with He used as a carrier gas. The following isotopes were measured at the low mass resolution mode ($m/\Delta m = 300$): ⁴⁹Ti, ⁵¹V, ⁵³Cr, ⁵⁵Mn, ⁵⁷Fe, ⁵⁹Co, ⁶⁰Ni, ⁶³Cu, ⁶⁶Zn, ⁷⁵As, ⁷⁷Se, ⁹⁵Mo, ¹⁰⁷Ag, ¹¹¹Cd, ¹²¹Sb, ¹²⁵Te, ²⁰⁸Pb and ²³⁸U. Trace elements data except Ti were calibrated against the synthetic polymetal sulfide MASS-1 (USGS) and the isotope ⁵⁷Fe was used as the internal standard assuming its concentration based on pyrite stoichiometry. Titanium was calibrated against the synthetic silicate standard glass NIST SRM 610. The time-resolved signal data of spot analyses were

processed using the Glitter software (van Achterbergh et al., 2001). The precision of the laser ablation analyses (1RSD) ranges between 5 and 15 % for most of the detected elements. The accuracy was monitored by a synthetic glass reference material STDGL3 (Belousov et al., 2016).

All the data handling and plotting were carried out by the GCDkit software (Janoušek et al., 2006).

5. Elemental redox proxies, modes of normalization and calculation of enrichment factors

Paleoredox conditions can be evaluated using a wide range of elemental, isotopic, and biomarker redox proxies (e.g., Tribouillard et al., 2005). Here, we will consider only C_{org}/P (an organic fraction proxy where C_{org} represents total organic carbon values TOC), theoretical degree of pyritization (DOP_T - an Fe speciation proxy), and trace-metal enrichment factors (EF).

Redox influence on recycling of sedimentary organic phosphorus was firstly recognized by Ingall and Jahnke (1994) and van Cappellen and Ingall (1994), but the pilot study that used C_{org}/P as a redox proxy was Algeo and Ingall (2007). Reducing facies generally yield $C_{org}/P > 100$ with peak values > 1000 , whereas oxidizing facies yield $C_{org}/P < 50$ with the lowest values < 10 (Algeo and Li, 2020 and references therein).

The DOP_T was defined by Algeo and Li (2020) as $DOP_T = S_T \times (55.85/64.12)/Fe_T$, where total sulfur (S_T) and total iron (Fe_T) substitute for Fe_{PY} and Fe_{HR} , respectively, and the coefficient 55.85/64.12 represents the weight ratio of Fe/S in stoichiometric pyrite. Because we have data for pyritic sulfur but no data for highly reactive iron, we use slightly adapted theoretical degree of pyritization (DOP_T) defined as $DOP_T = [S_{py} \times (55.85/64.12)/Fe_T]$ where pyrite sulfur (S_{py}) substitutes for total sulfur excluding the contribution of non-pyrite sulfur.

Algeo and Li (2020) concluded that it is likely that all DOP–DOP_T correlations are formation-specific, and these DOP_T thresholds cannot be applied to other formations without validation. They also noted the current use of inexact threshold of 0.7–0.8 as upper limit for ferruginous facies.

Many earlier studies used raw concentrations or bimetal ratios (e.g., V/Cr, V/(V+ Ni), and Ni/Co; Hatch and Leventhal, 1992; Jones and Manning, 1994). However, most of recent research favored Al-normalized enrichment factors (EF) using PAAS as the reference to evaluate trace metal enrichment (Tribovillard et al., 2006; Algeo and Tribovillard, 2009; Little et al., 2015; Sweere et al., 2016; Pašava et al., 2018; Algeo and Li, 2020). Nevertheless, Böning et al. (2012) and Little et al. (2015) documented that the impact of normalizing to the local lithogenic background rather than ‘average shale’ can be significant. Thus, as a reference material for calculation of enrichment factors we use a local lithogenic background represented by average graywacke (Supplementary Table 1) and calculate EF as $EF-X = [(X/Al)_{\text{sample}}/(X/Al)_{\text{graywacke}}]$ where X and Al represents concentration of given element and Al, respectively. An $EF > 1$ indicates authigenic enrichment of the given metal, while a value < 1 indicates depletion.

6. Results

6.1. U–Pb zircon and Re–Os pyrite geochronology

Zircon population of the LIB-ŠT-2 graywacke contains clear or rarely pale brown, mostly euhedral, both short- and long-prismatic or oval grains, 70–180 μm long. Oscillatory growth zoning is preserved in nearly all imaged grains together with sector zoning, but also irregular concentric zoning locally overprinted by zones of recrystallization or a new growth. The U–Pb dating of zircons yielded two prevailing distinct peaks. First cluster of ages yielded concordant ages scattering between ~535 Ma and 565 Ma (Supplementary Table 2) and this

spread of analyses provides weighted mean of $549 \text{ Ma} \pm 3 \text{ Ma}$ (32 analyses; Fig. 4). Second distinct cluster of ages constitute concordia age of $613 \pm 3 \text{ Ma}$ (MSWD = 3.8; probability 0.05, 19 analyses; Fig. 4). The remainder of dates are characterized by a minor inherited component at $\sim 685 \text{ Ma}$ (Tonian), Mesoproterozoic age is documented with a peak at $\sim 1.5 \text{ Ga}$ and also by Paleoproterozoic age at $\sim 2.0 \text{ Ga}$ (Supplementary Table 2; Fig. 4). The studied grains have Th/U ratios (Supplementary Table 2) of 0.3–1.4 (average 0.8).

The youngest U–Pb ages of zircon grains in populations of detrital zircons were used to constrain maximum depositional ages of the graywacke (Dickinson and Gehrels, 2009). For calculation of the youngest detrital zircons, a routine implemented in the Isoplot software (v 3.75; Ludwig, 2012) was used. The maximum depositional age calculated for sample LIB-ŠT-2 is $533 \pm 5/-6 \text{ Ma}$.

The Re–Os elemental and isotopic compositions of seven pyrite separates extracted from the black shales are given in Table 1. Altogether, the pyrites show a wide range of Re contents from ~ 3.82 to 83 ppb paralleled by radiogenic present-day $^{187}\text{Os}/^{188}\text{Os}$ between 2.24 and 6.15. The regression yields a Re–Os age of $307 \pm 16 \text{ Ma}$ with a significant degree of scatter (MSWD = 30) and an initial $^{187}\text{Os}/^{188}\text{Os}$ value of 0.87 ± 0.09 (Fig. 5).

6.2. Major and trace element compositions and enrichment factors

In terms of the major element compositions, the black shales and underlying graywackes mostly overlap with the exception of CaO, FeO, Na₂O and P₂O₅ contents being significantly higher in the graywackes (Table 2) reflecting different mineralogy of the both rock types (e.g., variable proportions of feldspar, apatite etc.). Yet, the most notable difference is total organic carbon (TOC or C_{org}) and sulfur contents ranging from 0.85 to 7.01 wt. % and 0.25 to 3.10 wt. % in the black shales, comparing to $<0.73 \text{ wt. \%}$ and $<0.05 \text{ wt. \%}$ in the graywackes,

respectively. Along the sampled profile, there is a continuous increase of Al/Fe_T paralleled by a decrease of TOC and S in the black shales (Fig. 6).

The C_{org}/P ratios range from ~144 to ~1293 (average ~575) in the black shales and between ~7 and ~31 (average ~15) in graywackes (Table 2). The DOP_T values yield a range of 0.01–0.79 (average ~0.26) and 0.001–0.008 (average 0.004) in the black shales and graywackes, respectively (Table 2). The calculated enrichment factors (EFs) of Mo, U, V, Cr, Ni, Co, Cu, Pb, Zn and As for black shales are given in Table 2 and selected EFs are also shown in Fig. 7. Authigenic enrichment in all samples was found for Mo (3–131, average 31), U (1–9, average 4), V (1–28, average 11) and Cr (1–26, average 6) whereas Ni, Co, As, Cu and Pb show both authigenic enrichment and depletion. No enrichment was found for Zn in our black shale sample set. In the black shales at the base of the Unit 2, high values of all EFs coincide with those of TOC, C_{org}/P, S_T, and DOP_T. Calculated Pearson linear correlation coefficients at the level of confidence of $p < 0.001$ (99.9%) ($n = 11$) show the highest positive correlations of TOC with V-EF, Pb-EF, U-EF, Mo-EF and Co-EF; DOP_T with Fe-EF and Ni-EF; and Mo-EF with Pb-EF, V-EF, U-EF and Fe-EF (Fig. 7) and also with DOP_T and S_{py} (at $p < 0.01$).

The Liblín black shales and graywackes exhibit similar, LREE-enriched chondrite-normalized (CN) rare earth element (REE) patterns ($La_N/Yb_N = 3.0–5.5$) with rather flat HREE distribution (Fig. 8), but the graywackes display more pronounced negative Eu anomaly comparing to the black shales ($Eu_{CN}/Eu_{CN}^* = 0.7–0.8$ and $0.8–0.9$). When normalized to PAAS, the black shales are characterized by largely positive Eu ($Eu_{PAAS}/Eu_{PAAS}^* = 1.2–1.6$) and mildly negative Ce ($Ce_{PAAS}/Ce_{PAAS}^* = 0.8–1.0$) anomalies. However, the black shale sample LIB-1/11 is exceptional, showing large negative Ce anomaly (Ce_{PAAS}/Ce_{PAAS}^* of 0.6) and Eu anomaly but no MREE fractionation (Fig. 8). Among other trace elements, the most striking feature is unusually high Ba enrichment detected in all black

shales from the sampled profile (up to ~10,500 ppm) comparing to the underlying graywackes (<620 ppm Ba) (Fig. 8) and U enrichment in the former (Table 2).

6.3. Iron, molybdenum, chromium and sulfur concentration and isotopic compositions

The iron, molybdenum, chromium and sulfur contents and their $\delta^{56}\text{Fe}$, $\delta^{98}\text{Mo}$ and $\delta^{53}\text{Cr}$ values are listed in Table 3.

Overall, the studied black shales as well as graywackes do not show any anomalous metal (e.g., Mo, Ni, Zn, V) contents and therefore, the Liblín black shales correspond to normal black shale (NBS) using the typology of Pašava (2000). The black shales are characterized by typically higher and variable Al/Fe_T decreasing downward along the sampled profile while the S contents increase up to 4.1 wt. %. Also, they yield very low and homogeneous distribution of Al/Mo due to rather high Mo contents (up to 72 ppm; Table 3), generally lower erratic Al/Cr and highly variable V/Cr when compared to the underlying graywackes (Fig. 6). The Cr-EF shows highest correlation with Ni-EF ($r = +0.98$), Fe-EF ($r = +0.87$) and S_{py} ($r = +0.90$) ($p < 0.001$, $n = 11$) and with the DOP_T and U-EF at $p < 0.01$ ($n = 11$). At the level of confidence of 95% ($p < 0.05$, $n = 11$), the Cr-EF is correlated with TOC and EFs of Cu, Mo, V, and S_T .

Black shales have on average lower $\delta^{56}\text{Fe}$ values (-0.35 to $+0.16$ ‰) and low Fe contents than graywackes with high $\delta^{56}\text{Fe}$ values ($+0.13$ to $+0.38$ ‰) and high Fe contents. Further, progressively heavier Fe isotopic signatures were detected with increasing depth (Fig. 6) in the black shales with the highest TOC and metal EFs values (e.g., Mo, U; Table 2). The Cr isotopic composition ($\delta^{53}\text{Cr}$) varies from -0.26 to $+0.77$ ‰ and -0.62 to $+0.13$ ‰ in the black shales and graywackes, respectively (Fig. 9). Significant correlation was found between $\delta^{53}\text{Cr}$ and V-EF ($r = +0.79$, $p < 0.01$, $n = 11$) and U-EF ($r = +0.62$, $p < 0.01$, $n = 11$). However, at a

closer look, two different groups in terms of $\delta^{53}\text{Cr}$ values can be recognized for the black shales: the predominant one with homogeneous, heavy $\delta^{53}\text{Cr}$ of $\sim +0.7\text{‰}$ paralleled by high Cr contents ($>85\text{ ppm}$) and another one with low Cr ($<59\text{ ppm}$) and $\delta^{53}\text{Cr}$ between -0.3 and $+0.1\text{‰}$ (Figs. 6 and 8). Molybdenum concentrations and values of Mo-EF in the Liblín black shales exhibit a large degree of variability from 3.4 to 72 ppm and from 3.2 to 130.5, respectively. Both values are well-correlated with TOC values ($r = +0.85$, $p < 0.001$, $n = 11$ and $r = +0.89$, $p < 0.001$, $n = 11$, respectively; Fig. 9) at rather low Mo/TOC ratios (< 10 ; except sample LIB-1/2) while all graywacke samples are characterized by very low Mo and TOC (Table 2). The Mo-EF values are strongly correlated with EFs of Pb ($r = +0.96$), V ($r = +0.93$), U ($r = +0.92$), Fe ($r = +0.85$) ($p < 0.001$, $n = 11$), and also with DOP_T and S_{py} at $p < 0.01$. The $\delta^{98}\text{Mo}$ values measured only in black shales range between $+0.38$ and $+0.98\text{‰}$ with a large scatter along the sampled section (Fig. 6). They show a positive correlation with EFs of As, Co and Pb at $p < 0.01$ and lower positive correlation with EFs of Mo, Co and Cu ($p < 0.05$) and also Mo abundances (Fig. 9). In comparison to all stable isotopic systems above, whole-rock $\delta^{34}\text{S}$ values occupy a rather restricted interval between $+3.0$ and $+10.9\text{‰}$ with no relationship to the whole rock sulfur contents. Total sulfur shows strong correlation with TOC and Co-EF ($r = +0.89$ and $+0.86$, respectively, $p < 0.001$, $n = 11$) and S_{py} with DOP_T , EFs of Fe, Ni, Cr, Co ($p < 0.001$, $n = 11$).

6.4. Trace element and sulfur isotopic composition of pyrite

Concentrations of selected trace elements of two types of pyrites (*Type I* and *II*; see Section 3 for more details) are summarized in Table 4 ($n = 1688$ in total). In general, both analyzed types show large variations of element contents (up to several orders of magnitude) between individual grains. Nevertheless, syngenetic pyrites (*Type I*) are distinguished

from recrystallized ones (*Type II*) by significantly higher median values of most analyzed metals (e.g., V, Cr, Mn, Mo) while Co is notably lower (5.6 vs. 66 ppm, respectively; Table 4, Fig. 10a, b). This resulted in much higher median Se/Co values detected in synsedimentary pyrites (~11) when compared to recrystallized type (~2.0). Levels of As, Ni, Pb, and Cu concentrations in the Type I pyrite (Fig. 10a) are well comparable with those of average sedimentary pyrite reported by Gregory et al. (2015), however, pyrite from Liblín is characterized by slightly higher Ag and Cd and much higher Sb and Zn values.

The $\delta^{34}\text{S}$ values in separated pyrites range from -12.2‰ (Type I, synsedimentary pyrite) to $+5.6\text{‰}$ (Type II, recrystallized pyrite) (Table 3).

7. Discussion

7.1. Timing of the black shale deposition and pyrite mineralization

Our combined U–Pb and Re–Os data provide new constraints on the depositional age of the black shales the associated pyrite mineralization, which have long been considered as Neoproterozoic in age (e.g., Pašava and Amov, 1993). However, the newly determined maximum depositional zircon age of the graywacke sample LIB-ŠT-2 is early Cambrian ($533 \pm 5\text{--}6\text{ Ma}$; Fig. 4), similar to an upper age limit determined at $534.8 \pm 3.5\text{ Ma}$ from another black shale horizon reported by Kurzweil et al. (2015). Despite the faulted contact between the dated graywacke and the main black shale horizon, both lithologies are frequently interbedded at Liblín. This observation suggests that they are parts of the same succession and their depositional ages are likely close to each other. The new U–Pb age determination is also consistent with recent studies of Hajná et al. (2017) and Žák et al. (2020) suggesting that growth of the Blovice accretionary complex continued until the early Cambrian. It is also important to note that our new depositional age for the Liblín black shales coincides with the Cambrian Explosion for which nutrient availability, oxygenation, and change of seawater

composition are commonly supposed to be the main environmental triggers (e.g., Boyle et al., 2014; Zhang et al., 2014; Dahl et al., 2019). This period was also metallogenetically important by deposition of high-TOC and high-U Alum black shales in Scandinavia (Andersson et al., 1985) and Ni–Mo–PGE–Au black shales in South China (Pašava et al., 2008; Han et al., 2015 and references therein).

In contrast to the maximum depositional age inferred from the U–Pb on zircon, the Re–Os age of 507 ± 16 Ma on pyrite (separates dominated by the coarse recrystallized pyrite) (Fig. 5) rather represents a younger thermal event of pyrite recrystallization (see below).

7.2. Depositional environment of the lower Cambrian black shales

Petrography and highly variable trace element and isotopic compositions of the sampled black shale interval reflect rapidly changing conditions of their depositional environment in terms of redox conditions, extent of terrigenous input, and degree of silicification. The analysis of redox state can be pursued through the elemental proxies as pioneered by Algeo and Maynard (2004) and further developed by e.g., Lyons and Severman (2006), Algeo and Tribovillard (2009), Tribovillard et al. (2006, 2012), Little et al. (2015) and Sweere et al. (2016). Recent review of Algeo and Liu (2020) evaluated 21 elemental proxies concluding that while no single proxy is a universally reliable redox indicator, some are more consistently useful than others, notably the TOC and trace metal EFs as discussed for the sampled black shales in detail below.

Enhanced preservation of organic C at lower redox potentials combined with higher sedimentary retention of re-mineralized organic P at higher redox potentials results in a strong relationship between benthic redox conditions and sedimentary C_{org}/P ratios (Algeo and Ingall, 2007). Under anoxic conditions, phosphorus is lost back to the water column leading to the sedimentary C_{org}/P ratios greater than the Redfield ratio (~ 106), whereas under oxic

conditions, phosphorus is retained in the sediment through adsorption onto Fe-oxyhydroxides leading to C_{org}/P ratios lower than the Redfield ratio (Algeo and Ingall, 2007; Kraal et al., 2012 and references therein). Our high C_{org}/P (up to ~1293) are close to that of the Upper Silurian–Lower Devonian graptolitic shales from Poland ($C_{\text{org}}/P = 151\text{--}1477$, mean 977, Porebska and Sawlowicz, 1997), collectively indicating prevalent anoxic depositional conditions. By contrast, the wide range of Mo values (3–72 ppm; Fig. 9) and EFs detected in the Liblín black shales indicate changes of non-euxinic with intermittently euxinic depositional conditions (e.g, Scott and Lyons, 2012). The latter is recorded at the base of the Unit 2 showing the peak EFs, DOP_T and C_{org}/P values (Fig. 7), but the lowest Al/Mo (Fig. 6) and Zr (detrital input). Positive correlations between different pairs of proxies and Mo-EF (Fig. 7) suggest that this multi-metal enrichment was contemporaneous rather than reflecting the obscured sequential onset relationship. Algeo and Tribovillard (2009) demonstrated strong Mo and U enrichments (EFs >10) of anoxic to euxinic facies, with enhanced enrichment of Mo_{auth} relative to U_{auth} at higher EFs (yielding progressively higher $(Mo/U)_{\text{sediment}}$ ratios, Table 2). Our dataset shows a positive Mo_{EF} intercept of ~9.4 at $U_{\text{EF}} = \sim 1.8$ (Fig. 11), indicating onset of Mo enrichment relative to U (similarly as reported from the Cariaco Basin, Framvaren Fjord, Saanich Inlet and other modern environments; Algeo and Li, 2020). Sediments of the Cariaco Basin exhibit strong enrichment of Mo relative to U at all EFs, reflecting the operation of a metal–oxyhydroxide particulate shuttle that enhances the export of aqueous Mo to the sediment (with little effect on U, Algeo and Tribovillard 2009). Thus, more reducing water mass conditions result in enrichment of the sediment in both U_{auth} and Mo_{auth} , but the rate of Mo uptake increases faster than that of U. At high Mo/U ratios, Mn-oxyhydroxide particulates generated at the redoxcline in open water columns (Berrang and Grill, 1974), can take up Mo as they sink and rapidly transfer it to the sediment/water interface (Algeo and Tribovillard, 2009; Dellwig et al., 2010). This process, which can lead to

Mo enrichment by the sediment with little uptake of U, reflects development of transient euxinia in the water column rather than more sustained euxinia in the sediment column (Algeo and Li, 2020). This is consistent with the euxinic depositional conditions of black shales at the base of Unit 2 (LIB-1/10 and 11), indicating a “particulate shuttle” trend.

Another explanation might be that Ediacaran-Cambrian seawater may have had a Mo/U ratio several times higher than modern seawater (T. Algeo, personal communication).

On the other hand, fluctuations of redox conditions along the rest of the sampled profile is documented by variable EFs (Fig. 7) and Mo/U relative to that of present-day seawater (SW) yielding a values between ~ 3 and $1 \times \text{SW}$ (Fig. 11).

We argue that the observed large variations in EFs reflect changes in redox conditions as a result of variable input of terrigenous material into the basin. For example, Mo is well correlated with TOC values ($r = +0.85$, $p < 0.001$, $n = 11$) and its authigenic component (calculated using the method of Little et al., 2016) is generally high ($> 92\%$ except few samples with low-TOC < 4 wt. % with M_{auth} between 77 and 87 %), suggesting predominant control by redox conditions with rather limited effect of terrigenous input on $\delta^{98}\text{Mo}$ systematics. Thus, largely variable $\delta^{98}\text{Mo}$ values from $+0.38$ to $+0.98\%$ with the most positive values detected in samples with the highest Mo-EF and Cr-EF (LIB-1/10 and 11) are in concert with the suggested variable redox conditions as inferred from EFs (see above). On the other hand, several lines of evidence indicate that Cr elemental and isotopic systematics were largely affected by terrigenous input in the Liblín black shales. For instance, largely variable Al/Cr paralleled by low Cr-EF values (down to ~ 1) indicates high Cr terrigenous component (up to 89 % calculated for LIB-1/7). Furthermore, chromium stable isotope systematics shows a high degree of variation from -0.26 to $+0.77\%$ with the lowest values overlapping with that of graywacke/siltstone (Fig. 6). On the other hand, there is a well-developed negative correlation between $\delta^{53}\text{Cr}$ values and negative Ce/Ce* values, which might

indicate reducing conditions of water column (e.g., German and Elderfield, 1990; Wignall, 1994). Strongly positive correlation between Cr-EF and some other EFs (e.g., Fe-EF, Co-EF, Ni-EF) seems to reflect entrapment of Cr with other metals during syndepositional pyrite formation (supported by higher Cr values in Type I pyrite – see Table 4). This implies that positive $\delta^{53}\text{Cr}$ values found in samples with lower terrigenous input ($< \sim 30\%$) and $\text{Cr-EF} > 3.5$ are related to prevalent reducing conditions during deposition.

Different slopes in the Mo vs. TOC curve were attributed to variable watermass renewal times (Algeo and Lyons, 2006). According to these authors, the low Mo/TOC ratios indicate limited availability of Mo_{aq} in more restricted basins. The lower the slope of indicative lines characterizing different modern settings the more depleted is the Mo_{aq} reservoir possibly due to restricted watermass circulation in the basin (Algeo and Lyons, 2006). The Liblín black shales are consistent with lower Mo_{aq} concentrations in the contemporaneous seawater and, thus, point to deposition in a transiently more restricted basin (Fig. 9). In principle, such transient restriction could result from changes in the ocean circulation pattern and/or water column stratification with sporadic venting like in the Gotland Deep of the Baltic Sea or the Saanich Inlet, Canada. Alternatively, physical changes in the sedimentary environment due to contemporary tectonic activity or temporal changes in the chemocline depth may have led to variations in ventilation and watermass exchange (Algeo and Lyons, 2006).

Overall, the Liblín black shales underwent significant silicification by low-temperature hydrothermal fluids producing the Si and Ba enrichments (up to 73.89 % SiO_2 and 1.05 % Ba), similar to what was already discussed in detail by Ackerman et al. (2021) for another black shale section from the Bohemian Massif. The detailed petrography revealed that this process was synchronous with black shale deposition therefore all relevant geochemical signs should be considered as primary. In this respect, the degree of anoxia as expressed, for instance, by TOC and EFs seems to be intimately connected with the extent of silicification

by Si–Ba–rich hydrothermal fluids. This is documented by the highest degree of silicification accompanied by very high TOC, S and Mo values including EFs of redox-sensitive metals in samples LIB-1/10 and 11 at the base of Unit 2 (Table 2, Fig. 6 and 7). This hydrothermal enrichment is consistent with precipitation of silica and barite from cooler fluids (~100–300 °C), which have been reported from vents distant from the heat source (e.g., Chevalloné, 1997; Judd and Hovland, 2007 and references therein).

Restricted new sulfur isotope data from synsedimentary/early diagenetic pyrite ($\delta^{34}\text{S} = -12.0\text{‰}$) and dominantly recrystallized pyrite (-1.1 to $+5.6\text{‰}$) are in agreement with results of previous studies of Hladíková et al. (1986) who reported $\delta^{34}\text{S}$ values in bulk pyrites of black shale at Liblín ranging from -1.7 to -19.5‰ . Negative $\delta^{34}\text{S}$ values require fractionation processes during sulfate reduction, during which the light ^{32}S is enriched in the sulfide phase. Considering the S isotopic composition of contemporaneous seawater sulfate during the Cambrian with $\delta^{34}\text{S}$ values around $+35\text{‰}$ (Claypool et al., 1980), the isotopic difference $\Delta^{34}\text{S}_{\text{sulfate-pyrite}}$ was up to 55‰ . This confirms that seawater sulfate concentrations were relatively high (Algeo et al., 2015). Such isotopic differences are relatively large but still in the range observed in modern marine sulfides (e.g., Canfield and Thamdrup, 1994; Jørgensen, 1990). Heavier $\delta^{34}\text{S}$ values in whole-rock (average $+7.0\text{‰}$) and local differences in sulfur isotopic composition between separated pyrite and whole-rock (-1.1‰ vs. $+2.9\text{‰}$, respectively, found in the middle part of the black shale section) most likely reflect heavier pore water sulfate.

7.3. A paradox of iron and $\delta^{56}\text{Fe}$ systematics

The Liblín black shales and underlying graywackes display different iron concentrations and isotopic compositions (Table 3 and Fig. 6), reflecting different metal sources and/or processes. The black shales are characterized by lower Fe_T concentrations (0.6 to 3.4 wt. %)

when compared to graywackes (2.6 to 5.4 wt. %), and also by much higher S contents. Together with the linear correlation between the Fe_T/Al and S ($r = 0.83$, $p < 0.01$, $n = 11$; Fig. 12), the Fe and S contents document authigenic pyrite enrichment, described previously by Kurzweil et al. (2015) in the nearby Neoproterozoic/Ediacaran black shales (Hromnice and Kamenec sites). However, only mild positive correlation between S and $\delta^{56}\text{Fe}$ values ($r = 0.58$, $p < 0.05$, $n = 11$; Fig. 12) indicates that the degree of sulfide precipitation does not control the extent of Fe isotopic fractionation to heavier values, which is also the case for $\delta^{98}\text{Mo}$ ($r = 0.51$, $p < 0.05$, $n = 11$; Fig. 9) and $\delta^{53}\text{Cr}$ (not plotted). More importantly, a significant correlation between $\delta^{56}\text{Fe}$ and Fe_T/Al ($r = 0.94$, $p < 0.05$, $n = 11$) is not consistent with either iron shuttling or with mixing of authigenic and detrital sources, because the authigenic Fe (high Fe_T/Al) enrichment in anoxic-anoxic settings is characterized by negative $\delta^{56}\text{Fe}$ (e.g., Dauphas et al., 2017; Severmann et al., 2006 and references therein) that are correlated with $\delta^{98}\text{Mo}$ values (e.g., Kurzweil et al., 2015). Also, the $\delta^{56}\text{Fe}$ values could not originate from hydrothermal metal enrichment as the Liblín black shales are poor in transition metals (e.g., Cu, Zn) and hydrothermal fluids tend to bear light $\delta^{56}\text{Fe}$ signatures (e.g., Sharma et al., 2001). Therefore, the opposite trend (“the Fe paradox”) found in the Liblín black shales suggests that some other process controlled the observed Fe isotopic fractionation.

The crucial insights into this phenomenon may come from the Fe_2O_3 and FeO bulk analyses combined from the petrography and field observations. Along the sampled section, Fe(III) continuously increases from the top to bottom (e.g. LIB-1/10 and 11), where silicified black shales show pyrite replacement (hydrothermal overprint by Si-Ba fluids). When omitting one sample with the anomalously high Fe_2O_3 contents (LIB-1/10), a well-defined positive correlation ($r = +0.78$, $p < 0.05$, $n = 10$) between Fe_2O_3 and $\delta^{56}\text{Fe}$ indicates that partial (bacterial?) oxidation of pyrites through the syndimentary hydrothermal circulation

of oxidizing fluids led to precipitation of isotopically heavy Fe-oxyhydroxides (e.g., Chever et al., 2015; Croal et al., 2004). Absence of any relationship between $\delta^{56}\text{Fe}$ values and redox proxies (e.g., EFs, TOC, $\delta^{98}\text{Mo}$) and between Si and/or Ba vs Mo and/or Cr imply that this process has not altered the redox proxies discussed in detail above.

7.4. Implications for oceanic and atmospheric oxygenation in the early Cambrian

As shown above, the high Mo contents preserved in the lowest part of the black shale horizon (with the negligible terrigenous input of Mo, samples LIB-1/10 and LIB-1/11) are well correlated with TOC and therefore, can be considered as authigenic. Unlike Fe systematics, the absence of any correlation between Mo systematics and hydrothermal silicification markers (e.g., SiO_2 , Ba, Fe_2O_3) suggests that this process did not contribute to the observed $\delta^{98}\text{Mo}$ signature. If true, the maximum recorded $\delta^{98}\text{Mo}$ values might be used as the best approximate of the ancient local seawater Mo composition (taking into account rather temporally restricted nature of the basin with limited access to the open sea) and contribute to the ongoing discussion on the ocean oxygenation in the past. According to Chen et al. (2015), $\delta^{98}\text{Mo}$ values approached $\sim 1.5\text{‰}$ around 550 Ma, and then reached $\sim 2\text{‰}$ for the first time in the Earth's history during the earliest Cambrian (~ 535 Ma, mid-Fortunian Stage). Our maximum $\delta^{98}\text{Mo}$ value ($+1.98\text{‰}$) is much lower than that determined in the ~ 530 Ma black shales from the Yangtze Platform, China (Wen et al., 2015), but identical to the value obtained from the nearby $\sim 560\text{--}535$ Ma black shales ($+0.95\text{‰}$) by Kurzweil et al. (2015). Thus, the data from the Liblín black shales argue against deep-ocean oxygenation in early Cambrian.

An extent of the Earth's atmosphere oxygenation can be deciphered through the in-situ LA-ICPMS trace element analyses of syngenetic pyrite (e.g., Large et al., 2014;

Steadman et al., 2020 and references therein). The determination of pyrite origin is important as it is only the small syngenetic (typically framboidal) and early diagenetic types of pyrite that retain the trace element signature of coeval seawater (Large et al., 2014; Gregory et al., 2015). In this respect, we are using only syngenetic and early diagenetic pyrite (Type I; Table 4, Fig. 10a) for further O₂ estimates. Both Se and Co are redox sensitive, but in opposite directions, and therefore, the Se/Co ratios in syngenetic pyrite acts as a highly sensitive atmosphere pO₂ proxy (Large et al., 2017) as already demonstrated by Large et al. (2019) for a detailed dataset of marine pyrite from the Devonian to Carboniferous periods. The evolution of Co and Se concentrations was demonstrated by the pyrite time-series curves (Large et al., 2019), where the marine pyrite exhibits increase of Se while Co contents generally falls over time from ~3600 Ma to the present. Combined results from two independent methods (measurement of oxygen concentrations in sedimentary halite/ooids and Se/Co ratio determinations in sedimentary pyrite grains from 310 black shale samples; see Steadman et al., 2020 for more details) derive the following relationship for the estimate of atmospheric oxygen concentrations:

$$\text{Atmospheric O}_2 \% = 30 \times [10^P / (1+P)] \quad (1)$$

where $P = 10^{[0.89 \times \log(\text{Se}/\text{Co}) + 0.07]}$, $t_4 = 4.91$, $p = 0.008$, $r^2 = 0.86$. When applying this equation for the Liblín section, we obtain estimated O₂ levels from ~18 to 29 % (minimum and maximum values, respectively) with the identical median and mean values of $\sim 27 \pm 2$ %.

For comparison, we also used improved calculation of Large et al. (2019):

$$\text{Atmospheric O}_2 \% = 8.5 \times \log(\text{Se}/\text{Co}) + 16.2; p = 0.1, r^2 = 0.94, \quad (2)$$

that includes a generally accepted estimate of O₂ < 0.02 wt.% at 3600 Ma (e.g., Lyons et al., 2014). This calculation yielded similar results with a range of O₂ values (~17–29 %), median value (~25 %) and a mean value of 25 ± 3 %.

Large et al. (2019) suggested that the Cambrian Explosion was associated with both a steep rise of micronutrients and concurrent rise of atmospheric O₂ from about 2 to 25 %, peaking at ~525 Ma and soon dropping to as low as ~3 % O₂ at 500 Ma. In this respect, our O₂ estimate from the Liblín synsedimentary pyrite is consistent with conclusions of Steadman et al. (2020) that O₂ rose gradually throughout the Ediacaran to reach a maximum of 20 to 29 % in the early Cambrian. By contrast, it is largely different from that of Dahl et al. (2019) who suggested much lower O₂ values (~ 4 %) at ~533 Ma derived from a complex isotopic study of marine carbonates and associated sedimentary successions. This discrepancy might be partly associated with limitations of our atmospheric oxygen estimates. These limitations include (1) errors/variability in measurement of oxygen in the halite fluid inclusions (Steadman et al., 2020), (2) the precision of the laser ablation analyses (1RSD), which varies from 5 to 15% and (3) natural heterogeneity of sedimentary pyrite related to trace element adsorption, and diagenetic/metamorphic modifications (e.g., Huerta-Diaz and Morse, 1992).

7.5. Tectonic controls on the black shale deposition

As argued above, the geochemical signatures of the Liblín black shales reflect a temporally decreased terrigenous supply to the basin from a nearby arc, basin subsidence, as well as the hydrothermal enrichment in Si and Ba. To put the geochemical data in a broader tectonic context, we propose the following model for evolution of the Liblín black shales.

The arc-derived graywackes were presumably deposited along the accretionary wedge surface through distal turbiditic flows (Fig. 13a; see also Hajná et al., 2013). In contrast, deposition of the black shales requires ephemeral deepening (subsidence) of the basin, which is difficult to explain in an overall compressional environment of the accretionary wedge. To explain periods of intermittent subsidence, we adopt a recent model of Normand et al. (2019). They suggested that during seismic slip on the subduction zone megathrusts, the upper

surfaces of accretionary wedges might undergo extension, whereas during inter-seismic periods, the megathrust surface is locked and the wedge is in compression. This mechanism would explain well the presence of thin black shale horizons (representing short-lived basin subsidence, Fig. 13b) within orders-of-magnitude thicker graywacke packages (representing the predominant wedge compression, Fig. 13a).

The subsidence resulted in the deposition of black shales under reducing conditions but was also accompanied by extensive upward percolation (along faults?) of hydrothermal fluids (Fig. 13b) resulting in low-temperature Si–Ba venting and increased biological productivity. This is evidenced by the deposition of high-TOC pyritic black shale at the base of the sequence (e.g., sample LIB-1/11), primary silicification (Fig. 3b,c), and anomalously high Ba contents (Table 2). Strongly negative values of $\delta^{34}\text{S}$ in pyrite confirm bacterial reduction of marine sulfate. The heat source that triggered the hydrothermal circulation in an overall cold environment of the accretionary wedge remains elusive. Yet, a subduction of a hot oceanic plate (ridge or plume) beneath the Blovice accretionary wedge during the waning stages of its evolution was invoked in several prior studies (e.g., Ackerman et al., 2019a; Hajná et al., 2018, 2017; Sláma et al., 2008) and is in agreement with the model presented here.

Deposition of the high-TOC black shales was apparently followed by a more chaotic deposition, which is documented by black shales with variable TOC and input of terrigenous material and restricted hydrothermal overprint (generally lower silicification towards the top of the section). The former is evidenced by changes in the redox conditions expressed by largely variable EFs and $\delta^{98}\text{Mo}$ and $\delta^{53}\text{Cr}$ values (Figs. 7 and 9) that very likely reflect different periods of temporally restricted basin. Enhanced flux of arc-derived material resulted in low Mo/TOC while higher Mo/TOC indicate more restricted period with more reducing conditions characterized by highly positive $\delta^{98}\text{Mo}$ and $\delta^{53}\text{Cr}$ values.

Recrystallization of synsedimentary/early diagenetic framboidal pyrite to coarse-grained pyrite grains/aggregates dominantly bound to quartz veins was dated at 507 ± 16 Ma (this study). This thermal event temporally overlaps with emplacement of voluminous granitic plutons into the accretionary complex in several pulses between ~ 524 and 505 Ma, interpreted as recording post-accretionary slab break-off and transition to an extensional regime (e.g., Dörr et al., 1998, 2002).

8. Conclusions

1. The newly determined maximum depositional zircon U–Pb age of the footwall graywackes indicates that the Liblín black shales were deposited at around 533 Ma, during early Cambrian. The Re–Os age of pyrite is slightly younger (507 ± 16 Ma) and indicative of a younger recrystallization event.
2. Based on the chemistry of major/trace elements and Mo–Cr systematics, these facies represent normal black shale (i.e. non-highly metalliferous facies) were deposited in an extensional trench-slope basin as result of tectonic subsidence. The largely variable EFs, $\delta^{98}\text{Mo}$ and ^{53}Cr values reflect changing redox conditions and varying siliciclastic input from the volcanic arc. However, euxinic conditions are evidenced by the highest values of C_{org}/P , DOP_T , Fe_T/Al and EFs of Mo, U and other redox-sensitive metals in the lowermost part of the sampled black shale section that yields highly positive $\delta^{98}\text{Mo}$ and ^{53}Cr values. Silica and Ba hydrothermal venting is confirmed by primary silicification and Ba-enrichment. Sulfur isotope values in pyrites are consistent with bacterial sulfate reduction of marine sulfate.
3. A lack of positive correlation between $\delta^{56}\text{Fe}$ and S and a strong relationship between

the $\delta^{56}\text{Fe}$ and Fe_2O_3 values indicate that Fe isotopic fractionation was not controlled by the degree of sulfide precipitation, but most likely reflects partial (bacterial?) oxidation of pyrites via the synsedimentary hydrothermal venting, which resulted in precipitation of isotopically heavy Fe-oxyhydroxides. Synsedimentary pyrite has higher mean As, Ag, Cr, Mn, Pb, Sb and V concentrations when compared to recrystallized one, which is, however characterized by higher mean Co, Cu and Se contents.

4. Finally, our calculations of oxygen levels based on redox-sensitive elements (Se/Co) in synsedimentary pyrite indicate the range of atmosphere O_2 values between ~17 and 29% (mean ~27%), supporting a previous hypothesis that O_2 content rose in the Ediacaran and reached a maximum of 20 to 29 % in the early Cambrian.

Acknowledgements

This study is a contribution to the Czech Science Foundation projects 17-15700S and 20-13644S (to LA) and to the Institutional support RVO67985831 of the Institute of Geology of the Czech Academy of Sciences and the DKRVO (2018–2022) of the Czech Geological Survey. Additional support was provided by the Charles University through projects PROGRES Q45 and Center for Geosphere Dynamics (UNCE/SCI/006) to JŽ. Pivovar Chříč is highly appreciated for hospitality during fieldwork. We also greatly appreciate useful reviews by Ross Large, Thomas Algeo and an anonymous reviewer that helped to improve the final version of the manuscript. We also thank T. Algeo for his efficient editorial handling.

References

- Ackerman, L., Pašava, J., Šípková, A., Martínková, E., Haluzová, E., Rodovská, Z., Chrastný, V., 2019a. Copper, zinc, chromium and osmium isotopic compositions of the Teplá–Barrandian unit black shales and implications for the composition and oxygenation of the Neoproterozoic–Cambrian ocean. *Chem. Geol.* 521, 59–75.
- Ackerman, L., Hajná, J., Žák, J., Erban, V., Sláma, J., Polák, L., Kachlík, V., Strnad, L., Trubač, J., 2019b. Architecture and composition of ocean floor subducted beneath northern Gondwana during Neoproterozoic to Cambrian: A palinspastic reconstruction based on Ocean Plate Stratigraphy (OPS). *Gondwana Res.* 76, 77–97.
- Ackerman, L., Pašava, J., Žák, J., Žák, K., Kachlík, V., Šebek, O., Trubač, J., Svojtka, M., Veselovský, F., Strnad, L., Santolík, V., 2021. Are related black shales as sedimentary archives of sea-level fluctuations and plate tectonics during the late Neoproterozoic: An example from the Bohemian Massif. *Mar. Pet. Geol.* 123, 104713.
- Algeo T.J., Maynard J.B., 2004. Trace-element behavior and redox facies in core shales of Upper Pennsylvanian Kansas-type cyclothems. *Chem. Geol.* 206, 289–318.
- Algeo, T.J., Lyons, T.W., 2006. Mo–total organic carbon covariation in modern anoxic marine environments: Implications for analysis of paleoredox and paleohydrographic conditions. *Paleoceanography* 21, PA1016.
- Algeo, T.J., Tribovillara, N., 2009. Environmental analysis of paleoceanographic systems based on molybdenum–uranium covariation. *Chem. Geol.* 268, 211–225.
- Algeo T.J., Ingall, E., 2007. Sedimentary $C_{org}:P$ ratios, paleocean ventilation, and Phanerozoic atmospheric pO_2 . *Palaeogeogr. Palaeoclimatol. Palaeoecol.* 256, 130–155
- Algeo, T.J., Luo, G.M., Song, H.Y., Lyons, T.W. and Canfield, D.E., 2015. Reconstruction of secular variation in seawater sulfate concentrations. *Biogeosci.* 12, 2131–2151.
- Algeo, T.J., Li, C., 2020. Redox classification and calibration of redox thresholds in sedimentary systems. *Geochim. Cosmochim. Acta* 287, 8–26.

- Algeo, T.J., Liu, J., 2020. A re-assessment of elemental proxies for paleoredox analysis. *Chem. Geol.* 540, 119549.
- Anbar, A.D., Duan, Y., Lyons, T.W., Arnold, G.L., Kendall, B., Creaser, R.A., Kaufman, A.J., Gordon, G.W., Scott, C., Garvin, J., Buick, R., 2007. A whiff of oxygen before the great oxidation event? *Science* 317, 1903–1906.
- Andersson, A., Dahlman, B., Gee, D.E., Snall, S., 1985. The Scandinavian Alum shales, Serie Ca, No. 56, Sveriges Geologiska Undersökning.
- Archer, C., Vance, D., 2008. The isotopic signature of the global riverine molybdenum flux and anoxia in the ancient oceans. *Nat. Geosci.* 1, 597–600.
- Arthur, M.A., Sageman, B.B., 1994. Marine black shales: Depositional mechanisms and environments of ancient deposits. *Annu. Rev. Earth Planet. Sci.* 22, 499–551.
- Bau, M., 1996. Controls on the fractionation of isovalent trace elements in magmatic and aqueous systems: Evidence from Y/Nb, Zr/Hf, and lanthanide tetrad effect. *Contrib. Mineral. Petrol.* 123, 323–333.
- Belousov, I., Large, R.R., Meffre, S., Danyushevsky, L.V., Steadman, J., Beardsmore, T., 2016. Pyrite compositions from VHMS and orogenic Au deposits in the Yilgarn Craton, Western Australia: Implications for gold and copper exploration. *Ore Geol. Rev.* 79, 474–499.
- Berrang, P.G., Grill, E.V., 1974. The effect of manganese oxide scavenging on molybdenum in Saanich Inlet, British Columbia. *Mar. Chem.* 2, 125–148.
- Berner, R.A., 2006. GEOCARBSULF: A combined model for Phanerozoic atmospheric O₂ and CO₂. *Geochim. Cosmochim. Acta.* 70, 5653–5664.
- Berner, Z.A., Puchelt, H., Nöltner, T., Kramar, U., 2013. Pyrite geochemistry in the Toarcian Posidonia Shale of south-west Germany: Evidence for contrasting trace-element patterns of diagenetic and syngenetic pyrites. *Sedimentology* 60, 548–573.

- Blamey, N.J.F., Brand, U., Parnell, J., Spear, N., Benison, K., Lecuyer, C., Meng, F., Ni, P., 2016. Paradigm shift in determining Neoproterozoic oxygen. *Geology* 44, 651–654.
- Blamey N.J.F., Brand, U., 2019. Atmospheric gas in modern and ancient halite fluid inclusions: A screening protocol. *Gondwana Res.* 69, 163–176.
- Böning, P., Fröllje, H., Beck, M., Schnetger, B., Brumsack, H.J., 2012. Underestimation of the authigenic fraction of Cu and Ni in organic-rich sediments. *Mar. Geol.* 323–325, 24–28
- Boyle, R. A., Dahl, T.W., Dale, A.W., Shields-Zhou, G.A., Zhu, M., Brasier, M.D., Lenton, T.M., 2014. Stabilization of the coupled oxygen and phosphorus cycles by the evolution of bioturbation. *Nature Geosci.* 7, 671–676.
- Boynton, W.V., 1984. Cosmochemistry of the rare earth elements: meteorite studies, in: Henderson, P. (Ed.), *Rare Earth Element Geochemistry*. Elsevier, Amsterdam, pp. 63–114.
- Calvert, S.E., Pedersen, T.F., 1993. Geochemistry of recent oxic and anoxic marine sediments: Implications for the geological record. *Mar. Geol.* 113, 67–88.
- Canfield, D.E., Poulton, S.W., Narbonne, G.M., 2007. Late-Neoproterozoic deep-ocean oxygenation and the rise of animal life. *Science* 315, 92–95.
- Canfield, D.E., Thamdrup, B., 1994. The production of ^{34}S -depleted sulfide during bacterial disproportionation of elemental sulfur. *Science* 266, 1973–1975.
- Chen, X., Ling, H.-F., Vance, D., Shields-Zhou, G.A., Zhu, M., Poulton, S.W., Och, L.M., Jiang, S.-Y., Li, D., Cremonese, L., 2015. Rise to modern levels of ocean oxygenation coincided with the Cambrian radiation of animals. *Nat. Commun.* 6, 7142.
- Chevaldonné, P., 1997. The fauna at deep-sea hydrothermal vents, an introduction, in: Desbruyeres, D., Segonzac, M. (Eds.), *Handbook of Deep-Sea Hydrothermal Vent Fauna*. IFREMER, Plouzane, France, pp. 7–20.

- Chever, F., Rouxel, O.J., Croot, P.L., Ponzevera, E., Wuttig, K., Auro, M., 2015. Total dissolvable and dissolved iron isotopes in the water column of the Peru upwelling regime. *Geochim. Cosmochim. Acta* 162, 66–82.
- Claypool, G.E., Holser, W.T., Kaplan, I.R., Sakai, H., Zak, I., 1980. The age curves of sulfur and oxygen isotopes in marine sulfate and their mutual interpretation. *Chem. Geol.* 28, 199–260.
- Craddock, P.R., Dauphas, N., 2011. Iron isotopic compositions of geological reference materials and chondrites. *Geostand. Geoanalytical Res.* 35, 101–123.
- Croal, L.R., Johnson, C.M., Beard, B.L., Newman, D.K., 2004. Iron isotope fractionation by Fe(II)-oxidizing photoautotrophic bacteria. *Geochim. Cosmochim. Acta* 68, 1227–1242.
- Dahl, T.W., Connelly, J.N., Li, D., Kouchinsky, A., Gill, B.C., Porter, S., Maloof, A.C., Bizzarro, M., 2019. Atmosphere-ocean oxygen and productivity dynamics during early animal radiations. *Proc. Natl. Acad. Sci.* 116, 19352–19361.
- Dauphas, N., John, S.G., Rouxel, O., 2017. Iron isotope systematics. *Rev. Mineral. Geochem.* 82, 415–510.
- Dellwig, O., Leipe, T., März, C., Glockzin, M., Pollehne, F., Schnetger, B., Yakushev, E.V., Bottcher, M.E., Brumsack, H.J., 2010. A new particulate Mn–Fe–P-shuttle at the redoxcline of anoxic basins. *Geochim. Cosmochim. Acta* 74, 7100–7115.
- Dempírová, L., Šíkl, J., Kašičková, R., Zoulková, V., Kříbek, B., 2010. The evaluation of precision and relative error of the main components of silicate analyses in Central Laboratory of the Czech Geological Survey. *Geosci. Res. Rep.* 27, 326–330.
- Dickinson, W.R., Gehrels, G.E., 2009. Use of U–Pb ages of detrital zircons to infer maximum depositional ages of strata: A test against a Colorado Plateau Mesozoic database. *Earth Planet. Sci. Lett.* 288, 115–125.
- Dörr, W., Fiala, J., Franke, W., Haack, U., Philippe, S., Schastok, J., Scheuven, D., Vejnar,

- Z., Zulauf, G., 1998. Cambrian vs. Variscan tectonothermal evolution within the Teplá–Barrandian: evidence from U–Pb zircon ages of syntectonic plutons (Bohemian Massif, Czech Republic). *Acta Univ. Carolinae, Geol.* 42, 229–230.
- Dörr, W., Zulauf, G., Fiala, J., Franke, W., Vejnar, Z., 2002. Neoproterozoic to Early Cambrian history of an active plate margin in the Teplá–Barrandian unit: a correlation of U–Pb isotopic-dilution-TIMS ages (Bohemia, Czech Republic). *Tectonophysics* 352, 65–85.
- El Korh, A., Luais, B., Deloule, E., Cividini, D., 2017. Iron isotope fractionation in hydrothermally altered high-pressure metabasites (Ile de Croix, France). *Contrib. Mineral. Petrol.* 172, 41.
- Fairchild, I.J., Kennedy, M.J., 2007. Neoproterozoic glaciation in the Earth system. *J. Geol. Soc. London* 164, 895–921.
- Farkaš, J., Chrástný, V., Novák, M., Čadkova, E., Pašava, J., Chakrabarti, R., Jacobsen, S.B., Ackerman, L., Bullen, T.D., 2013. Chromium isotope variations ($\delta^{53/52}\text{Cr}$) in mantle-derived sources and their weathering products: Implications for environmental studies and the evolution of $\delta^{53/52}\text{Cr}$ in the Earth's mantle over geologic time. *Geochim. Cosmochim. Acta* 122, 71–92.
- Fike, D.A., Grotzinger, J.P., Pratt, L.M., Summons, R.E., 2006. Oxidation of the Ediacaran ocean. *Nature* 444, 744–747.
- Franke, W., 2006. The Variscan orogen in Central Europe: Construction and collapse. *Geol. Soc. London Mem.* 32, 333–343.
- Franke, W., 2000. The mid-European segment of the Variscides: tectono-stratigraphic units, terranes boundaries and plate tectonic evolution. *Geol. Soc. London Spec. Publ.* 179, 35–61.
- Gaspers, N., Magna, T., Ackerman, L., 2020. Molybdenum mass fractions and stable isotope

- compositions of sedimentary carbonate and silicate reference materials. *Geostand. Geoanalytical Res.* 44, 363–374.
- German, C.R., Elderfield, H., 1990. Application of the Ce anomaly as a paleoredox indicator: The ground rules. *Paleoceanography* 5, 823–833.
- Hajná, J., Žák, J., Kachlík, V., Chadima, M., 2012. Deciphering the Variscan tectonothermal overprint and deformation partitioning in the Cadomian basement of the Teplá–Barrandian unit, Bohemian Massif. *Int. J. Earth Sci.* 101, 1855–1873.
- Hajná, J., Žák, J., Kachlík, V., Dörr, W., Gerdes, A., 2013. Neoproterozoic to early Cambrian Franciscan-type mélanges in the Teplá–Barrandian unit, Bohemian Massif: Evidence of modern-style accretionary processes along the Cadomian active margin of Gondwana? *Precambrian Res.* 224, 653–670.
- Hajná, J., Žák, J., Dörr, W., 2017. Time scales and mechanisms of growth of active margins of Gondwana: A model based on detrital zircon ages from the Neoproterozoic to Cambrian Blovice accretionary complex, Bohemian Massif. *Gondwana Res.* 42, 63–83.
- Hajná, J., Žák, J., Dörr, W., Kachlík, V., Sláma, J., 2018. New constraints from detrital zircon ages on prolonged, multiphase transition from the Cadomian accretionary orogen to a passive margin of Gondwana. *Precambrian Res.* 317, 159–178.
- Hajná, J., Žák, J., Ackerman, L., Svojtka, M., Pašava, J., 2019. A giant late Precambrian chert-bearing olistostrome discovered in the Bohemian Massif: a record of Oceanic Plate Stratigraphy (OPS) disrupted by mass-wasting along an outer trench slope. *Gondwana Res.* 74, 173–188.
- Haluzová, E., Ackerman, L., Pašava, J., Jonášová, Š., Svojtka, M., Hrstka, T., Veselovský, F., 2015. Geochronology and characteristics of Ni–Cu–(PGE) mineralization at Rožany, Lusatian granitoid complex, Czech Republic. *J. Geosci.* 60, 219–236.
- Han, T., Zhu, X., Li, K., Jiang, L., Zhao, C., Wang, Z., 2015. Metal sources for the

- polymetallic Ni–Mo–PGE mineralization in the black shales of the Lower Cambrian Niutitang Formation, South China. *Ore Geol. Rev.* 67, 158–169.
- Hatch, J.R., Leventhal, J.S., 1992. Relationship between inferred redox potential of the depositional environment and geochemistry of the Upper Pennsylvanian (Missourian) Stark Shale Member of the Dennis Limestone, Wabaunsee County, Kansas, U.S.A. *Chem. Geol.* 99, 65–82.
- Hladíková, J., Šmejkal, V., Pašava, J., Breiter, K., 1986. Isotopes of sulphur, carbon and oxygen at selected localities of the Barrandian Proterozoic. *Bulletin of the Central Geological Survey* 61, 339–348.
- Hoffman, P.F., Kaufman, A.J., Halverson, G.P., Schrag, D.P., 1998. A Neoproterozoic Snowball Earth. *Science* 281, 1342–1346.
- Huerta-Diaz, M., Morse, J.W., 1992. Pyritization of trace metals in anoxic marine sediments. *Geochim. Cosmochim. Acta* 56, 2661–2702.
- Ingall, E., Jahnke, R., 1994. Evidence for enhanced phosphorus regeneration from marine sediments overlain by oxygen depleted waters. *Geochim. Cosmochim. Acta* 58, 2571–2575.
- Janoušek, V., Farrow, C.M., Elban, V., 2006. Interpretation of whole-rock geochemical data in igneous geochemistry: Introducing Geochemical Data Toolkit (GCDkit). *J. Petrol.* 47, 1255–1259.
- Jones, B., Manning, D.A.C., 1994. Comparison of geochemical indices used for the interpretation of palaeoredox conditions in ancient mudstones. *Chem. Geol.* 111, 111–129.
- Jørgensen, B.B., 1990. A thiosulfate shunt in the sulfur cycle of marine sediments. *Science* 249, 152–154.
- Judd, A., Hovland, M., 2007. *Seabed Fluid Flow: The Impact on Geology, Biology and the*

- Marine Environment. Cambridge University Press, Cambridge.
- Kendall, B., Dahl, T.W., Anbar, A.D., 2017. The stable isotope geochemistry of molybdenum. *Rev. Mineral. Geochem.* 82, 683–732.
- Kraal, P., Slomp, C.P., Reed, D.C., Reichart, G.J., Poulton, S.W., 2012. Sedimentary phosphorus and iron cycling in and below the oxygen minimum zone of the northern Arabian Sea. *Biogeosci.* 9, 2603–2624.
- Kurzweil, F., Drost, K., Pašava, J., Wille, M., Taubald, H., Schoeckle, D., Schoenberg, R., 2015. Coupled sulfur, iron and molybdenum isotope data from black shales of the Teplá–Barrandian unit argue against deep ocean oxygenation during the Ediacaran. *Geochim. Cosmochim. Acta* 171, 121–142.
- Large, R.R., Halpin, J.A., Danyushevsky, L.V., Maslennikov, V.V., Bull, S.W., Long, J.A., Gregory, D.D., Lounejeva, E., Lyons, T.W., Seck, P.J., McGoldrick, P.J., Calver, C.R., 2014. Trace element content of sedimentary pyrite as a new proxy for deep-time ocean–atmosphere evolution. *Earth Planet. Sci. Lett.* 389, 209–220.
- Large, R.R., Mukherjee, I., Gregory, D., Steadman, J., Corkrey, R., Danyushevsky, L.V., 2019. Atmosphere oxygen cycling through the proterozoic and phanerozoic. *Miner. Depos.* 54, 485–506.
- Li, Z.X., Bogdanova, S.V., Collins, A.S., Davidson, A., De Waele, B., Ernst, R.E., Fitzsimons, I.C.W., Fuck, R.A., Gladkochub, D.P., Jacobs, J., Thrane, K., Vernikovskiy, V., 2008. Assembly, configuration, and break-up history of Rodinia: A synthesis. *Precambrian Res.* 160, 179–210.
- Liu, P.P., Zhou, M.F., Luais, B., Cividini, D., Rollion-Bard, C., 2014. Disequilibrium Fe isotope fractionation during the high-temperature magmatic differentiation of the Baima Fe–Ti oxide-bearing mafic intrusion, SW China. *Earth Planet Sci Lett* 339, 21–29.
- Linnemann, U., Gerdes, A., Hofmann, M., Marko, L., 2014. The Cadomian Orogen:

- Neoproterozoic to Early Cambrian crustal growth and orogenic zoning along the periphery of the West African Craton: Constraints from U–Pb zircon ages and Hf isotopes (Schwarzburg Antiform, Germany). *Precambrian Res.* 244, 236–278.
- Little, S.H., Vance, D., Walker-Brown, C., Landing, W.M., 2014. The oceanic mass balance of copper and zinc isotopes, investigated by analysis of their inputs, and outputs to ferromanganese oxide sediments. *Geochim. Cosmochim. Acta* 125, 673–693.
- Little, S.H., Vance, D., Lyons, T.W., McManus, J., 2015. Controls on trace metal authigenic enrichment in reducing sediments: Insights from modern oxygen-deficient settings. *Am. J. Sci.* 315, 77–119.
- Lyons, T., Reinhard, C.T., Planavsky, N.J., 2014. The rise of oxygen in Earth's early ocean and atmosphere. *Nature* 506, 307–315.
- Marin-Carbonne, J., Rollion-Bard, C., Luais, F., 2011. In-situ measurements of iron isotopes by SIMS: MC-ICP-MS intercalibration and application to a magnetite crystal from the Gunflint chert. *Chem. Geol.* 285, 50–61.
- Marshall, C.R., 2006. Explaining the Cambrian “explosion” of animals, *Ann. Rev. Earth Planet. Sci.* 34, 355–384.
- Morelli, R.M., Bell, C.C., Creaser, R.A., Simonetti, A., 2010. Constraints on the genesis of gold mineralization at the Homestake Gold Deposit, Black Hills, South Dakota from rhenium–osmium sulfide geochronology. *Miner. Depos.* 45, 461–480.
- Moynier, F., Vance, D., Fujii, T., Savage, P., 2017. The isotope geochemistry of zinc and copper. *Rev. Mineral. Geochem.* 82, 543–600.
- Mukherjee, I., Large, R.R., Bull, S., Gregory, D.G., Stepanov, A.S., Ávila, J., Ireland, T.R., Corkrey, R., 2019. Pyrite trace-element and sulfur isotope geochemistry of paleo-mesoproterozoic McArthur Basin: Proxy for oxidative weathering. *Am. Mineral.* 104, 1256–1272.

- Nance, R.D., Murphy, J.B., Strachan, R.A., D'Lemos, R.S., Taylor, G.K., 1991. Late Proterozoic tectonostratigraphic evolution of the Avalonian and Cadomian terranes. *Precambrian Res.* 53, 41–78.
- Nance, R.D., Gutiérrez-Alonso, G., Keppie, J.D., Linnemann, U., Murphy, J.B., Quesada, C., Strachan, R.A., Woodcock, N.H., 2010. Evolution of the Rheic Ocean. *Gondwana Res.* 17, 194–222.
- Narbonne, G.M., 2005. The Ediacara biota: Neoproterozoic origin of animals and their ecosystems. *Ann. Rev. Earth Planet. Sci.* 33, 421–442.
- Normand, R., Simpson, G., Bahroudi, A., 2019. Extension at the coast of the Makran subduction zone (Iran). *Terra Nov.* 31, 503–510.
- Och, L.M., Shields-Zhou, G.A., 2012. The Neoproterozoic oxygenation event: Environmental perturbations and biogeochemical cycles. *Earth Sci. Rev.* 110, 26–57.
- Pašava, J., 2000. Normal versus metal-rich black shales in the Barrandian Neoproterozoic of the Teplá–Barrandian Unit: A summary with new data. *Bulletin of Geosciences* 75, 229–240.
- Pašava, J., Amov, B., 1993. Isotopic composition of lead in Proterozoic anoxic metasedimentary and volcanogenic rocks from the Bohemian Massif (Czech Republic) with metallogenic implications. *Chem. Geol.* 109, 293–304.
- Pašava, J., Hladíková, J., Dobeš, P., 1996. Origin of Proterozoic black shales from the Bohemian Massif, Czech Republic. *Econ. Geol.* 91, 63–79.
- Pašava, J., Kříbek, B., Vymazalová, A., Sýkorová, I., Žák, K., Orberger, B., 2008. Multiple sources of metals of mineralization in Lower Cambrian black shales of South China: Evidence from geochemical and petrographic study. *Resour. Geol.* 58, 25–42.
- Pašava, J., Chrastný, V., Loukola-Ruskeeniemi, K., Käpyaho, A., Šebek, O., 2019. Nickel

- isotopic variation in black shales from Bohemia, China, Canada, and Finland. *Miner. Depos.* 54, 719–742.
- Pašava, J., Veselovský, F., Pour, O., Ackerman, L., Svojtka, M., Creaser, R.A., 2019. Timing and composition of stratiform pyrite mineralization in black shales at Liblín (Teplá–Barrandian Unit, Bohemian Massif), in: *Proceedings of the 15th SGA Biennial Meeting. Society for Geology Applied to Mineral Deposits, Glasgow*, pp. 1437–1440.
- Paton, C., Hellstrom, J., Paul, B., Woodhead, J., Hergt, J., 2011. Iolite: Freeware for the visualisation and processing of mass spectrometric data. *J. Anal. At. Spectrom.* 26, 2508–2518.
- Peřestý, V., Lexa, O., Holder, R., Jeřábek, P., Racek, M., Štěpánková, P., Schulmann, K., Hacker, B., 2017. Metamorphic inheritance of Rheic passive margin evolution and its early-Variscan overprint in the Teplá–Barrandian Unit, Bohemian Massif. *J. Metamorph. Geol.* 35, 327–355.
- Peřestý, V., Lexa, O., Jeřábek, P., 2020. Restoration of early-Variscan structures exposed along the Teplá shear zone in the Bohemian Massif: Constraints from kinematic modelling. *Int. J. Earth Sci.* 109, 1189–1211.
- Peters, S.E., Gaines, R.R., 2012. Formation of the 'Great Unconformity' as a trigger for the Cambrian explosion. *Nature* 484, 363–366.
- Porebska, E., Sawlowicz, Z., 1997. Palaeoceanographic linkage of geochemical and graptolite events across the Silurian–Devonian boundary in Bardzkie Mountains (Southwest Poland). *Palaeogeogr. Palaeoclimatol. Palaeoecol.* 132, 343–354.
- Pin, C., Waldhausrová, J., 2007. Sm–Nd isotope and trace element study of Late Proterozoic metabasalts (“spilites”) from the Central Barrandian domain (Bohemian Massif, Czech Republic). *Geol. Soc. Am. Spec. Pap.* 423, 231–247.
- Qin, L., Wang, X., 2017. Chromium isotope geochemistry. *Rev. Mineral. Geochem.* 82, 379–

414.

- Roskosz, M., Luais, B., Watson, H.C., Toplis, M.J., Alexander, C.M.O. 'D., Mysen, B.O., 2006. Experimental quantification of the fractionation of Fe isotopes during metal segregation from a silicate melt. *Earth Planet. Sci. Lett.* 248, 851–867.
- Rosman, K.J.R., Taylor, P.D.P., 1998. Isotopic compositions of the elements. *J. Phys. Chem. Ref. Data* 27, 1275–1287.
- Schulmann, K., Konopásek, J., Janoušek, V., Lexa, O., Lardeaux, J.-M., Edel, J.-B., Štípská, P., Ulrich, S., 2009. An Andean type Palaeozoic convergence in the Bohemian Massif. *Comptes Rendus Geosci.* 341, 266–286.
- Severmann, S., Johnson, C.M., Beard, B.L., McManus, J., 2006. The effect of early diagenesis on the Fe isotope compositions of porewaters and authigenic minerals in continental margin sediments. *Geochim. Cosmochim. Acta* 70, 2006–2022.
- Sharma, M., Polizzotto, M., Anbar, A.D., 2011. Iron isotopes in hot springs along the Juan de Fuca Ridge. *Earth Planet. Sci. Lett.* 194, 39–51.
- Siebert, C., Kramers, J.D., Meisel, T., Morel, P., Nägler, T.F., 2005. PGE, Re–Os, and Mo isotope systematics in Archaean and early Proterozoic sedimentary systems as proxies for redox conditions of the early Earth. *Geochim. Cosmochim. Acta* 69, 1787–1801.
- Sláma, J., Dunkley, D.J., Kachlík, V., Kusiak, M.A., 2008. Transition from island-arc to passive setting on the continental margin of Gondwana: U–Pb zircon dating of Neoproterozoic metaconglomerates from the SE margin of the Teplá–Barrandian Unit, Bohemian Massif. *Tectonophysics* 461, 44–59.
- Steadman, J.A., Large, R.R., Blamey, N.J., Mukherjee, I., Corkrey, R., Danyushevsky, L.V., Maslennikov, V., Hollings, P., Garven, G., Brand, U., Brand, U., Lécuyer, C., 2020. Evidence for elevated and variable atmospheric oxygen in the Precambrian. *Precambrian Res.* 343, 105722.

- Strnad, L., Mihaljevič, M., Šebek, O., 2005. Laser ablation and solution ICP-MS determination of Rare Earth Elements in USGS BIR-1G, BHVO-2G and BCR-2G glass reference materials. *Geostand. Geoanalytical Res.* 29, 303–314.
- Sweere, T., van den Boorn, S., Dickson, A.J., Reichart, G.J., 2016. Definition of new trace-metal proxies for the controls on organic matter enrichment in marine sediments based on Mn Co, Mo and Cd concentrations. *Chem. Geol.* 441, 235–245.
- Taylor, S.R., McLennan, S.M., 1985. *The Continental Crust: Its Composition and Evolution*. Blackwell Publishing, Oxford.
- Tribovillard, N., Algeo, T.J., Lyons, T., Riboulleau, A., 2006. Trace metals as paleoredox and paleoproductivity proxies: An update. *Chem. Geol.* 232, 12–32.
- Tribovillard, N., Algeo, T.J., Baudin, F., Riboulleau, A., 2012. Analysis of marine environmental conditions based on molybdenum-uranium covariation: Applications to Mesozoic paleoceanography. *Chem. Geol.* 324–325, 46–58.
- van Achterbergh, E., Ryan, C.G., Jackson, S.E., Griffin, W.L., 2001. Data reduction software for LA-ICP-MS, in: Sylvester, P.J. (Ed.), *Laser-Ablation-ICPMS in the Earth Sciences: Principles and Applications*. Mineralogical Association of Canada, pp. 239–243.
- van Cappellen, P., Ingall, E.D., 1996. Redox stabilization of the atmosphere and oceans by phosphorus-limited marine productivity. *Science* 271, 493–496.
- Vance, D., Archer, C., Little, S.H., Köbberich, M., de Souza, G.F., 2017. The oceanic cycles of the transition metals and their isotopes. *Acta Geochim.* 36, 359–362.
- Wen, H., Fan, H., Zhang, Y., Cloquet, C., Carignan, J., 2015. Reconstruction of early Cambrian ocean chemistry from Mo isotopes. *Geochim. Cosmochim. Acta* 164, 1–16.
- Whitney, D.L., Evans, B.W., 2010. Abbreviations for names of rock-forming minerals. *Am. Mineral.* 95, 185–187.

- Wignall, P.B., 1994. *Black Shales*. Oxford University Press, New York.
- Willbold, M., Hibbert, K., Lai, Y.J., Freymuth, H., Hin, R.C., Coath, C., Vils, F., Elliott, T., 2015. High-precision mass-dependent molybdenum isotope variations in magmatic rocks determined by double-spike MC-ICP-MS. *Geostand. Geoanalytical Res.* 40, 389–403.
- Wille, M., Nebel, O., van Kranendonk, M.J., Schoenberg, R., Kleinhanns, I.C., Ellwood, M.J., 2013. Mo–Cr isotope evidence for a reducing Archean atmosphere in 3.46–2.76Ga black shales from the Pilbara, Western Australia. *Chem. Geol.* 340, 68–76.
- Yanagisawa, F., Sakai, H., 1983. Thermal decomposition of barium sulfate–vanadium pentaoxide–silica glass mixtures for preparation of sulfur dioxide in sulfur isotope ratio measurements. *Anal. Chem.* 55, 985–987.
- Zhang, X., Shu, D., Han, J., Zhang, Z., Liu, J., Fu, D., 2014. Triggers for the Cambrian explosion: Hypotheses and problems. *Gondwana Res.* 25, 896–909.
- Žák, J., Svojtka, M., Hajná, J., Ackerman, U., 2020. Detrital zircon geochronology and processes in accretionary wedges. *Earth Sci. Rev.* 207, 103214.

Figure captions

Fig. 1. (a) A paleotectonic map of the northern margin of Gondwana to show the plate-tectonic setting of the Blovice accretionary complex within the Avalonian–Cadomian belt during late Neoproterozoic to early Cambrian (modified from Ackerman et al., 2019). The Blovice accretionary complex underlies much of the Teplá–Barrandian unit (TBU); the neighboring units are Saxothuringian (SX), Armorican (AR) and Ossa Morena (OM). (b) An idealized cross-section through the former active margin of northern Gondwana with two sub-parallel subduction zones, the Blovice accretionary complex presumably formed above a subducting back-arc domain (after Ackerman et al., 2019b). (c) Simplified map of the Variscan orogenic belt in Western and Central Europe showing position of crustal fragments

with well-preserved Cadomian basement (modified from Hajná et al., 2018). (d) Geologic map of the Teplá–Barrandian unit and the Blovice accretionary complex, with its internal structure defined by alternating siliciclastic (mostly coherent) and mélangé, basalt-bearing belts (modified from Hajná et al., 2019, 2017). The accretionary complex was intruded by Cambrian plutons shortly after the end of accretion.

Fig. 2. (a) Geological map of the Liblín section and vicinity. The sampled section is located in the footwall of a Variscan reverse fault that separates different lithotectonic belts of the Blovice accretionary complex; the section is in the mélangé Belt 2 characterized by abundant basalt blocks within siliciclastic matrix. Based on detailed mapping by J. Žák and J. Hajná (unpublished data). (b) Cross-section through the Liblín section showing a stack of three main units, Units 1 and 3 are graywackes with various proportion of shale and siltstone interbeds, Unit 2 is the main black shale horizon. Despite the tectonic overprint, the original stratigraphic relationships and lithologic transitions have largely been preserved. (c) Field examples of Units 1–3 from the Liblín section.

Fig. 3. Photomicrographs of main lithological rock types and pyrites: (a) graywacke, (b) fine-grained laminated black shale, (c) black shale with primary silicification, (d) two types of pyrite – synsedimentary dispersed in Si-rich matrix (not quartz veins) and recrystallized, (e) silicified black shale with pyrite associated with barite, (f) progressing recrystallization of framboidal pyrite in siliceous black shale, (g) Fe-oxyhydroxide in black shale without coating pyrite grains and/or developing along fractures and intergranular spaces, suggesting their primary origin, (h) microinclusions of sphalerite and chalcopyrite in slightly recrystallized pyrite. Abbreviations: Brt – barite, Ccp – chalcopyrite, Plg – plagioclase, Py – pyrite, Qz – quartz, Sp – sphalerite (Whitney and Evans, 2010).

Fig. 4. Concordia $^{206}\text{Pb}/^{238}\text{U}$ vs $^{207}\text{Pb}/^{235}\text{U}$ age plot or the weighted mean age $^{206}\text{Pb}/^{238}\text{U}$ of laser ablation ICP-MS U–Pb analyses of studied zircons from the graywacke LIB-ŠT-2 (data-point error ellipses are 2σ) and histogram of zircon concordia age distributions. For data presentation, kernel density estimates (blue line) and frequency histograms with a bin width of 15 Ma and a bandwidth of 10 Ma were used (n denotes the number of analyses).

Fig. 5. Re–Os regression age for eight pyrites from pyritic black shales at Liblín.

Fig. 6. Distribution of total organic carbon (TOC), $\text{Fe}_2\text{C}_2/\text{S}$, Al/Mo, Al/Cr, Al/ Fe_T and $\delta^{98}\text{Mo}$, $\delta^{53}\text{Cr}$ and $\delta^{56}\text{Fe}$ values in detritic and pelagic sediments sampled along stratigraphy section at Liblín. Note that error bars for $\delta^{53}\text{Cr}$ are smaller than symbol size.

Fig. 7. (a) Distribution of major redox proxies ($\text{C}_{\text{org}}/\text{P}$, DOP_T and selected enrichments factors – Mo, U, V and Cr) in the pelagic sediments sampled across stratigraphy at Liblín. The highest values of all redox proxies are bound to black shales deposited under euxinic conditions at the base of the Unit 2 while the fluctuations of redox conditions along the rest of the sampled profile is documented by variable EFs and other proxies. (b) Simple co-variation and strong correlation between Mo-EF and EFs of other metals reflect most likely simultaneous co-enrichment of these proxies in response to reducing depositional conditions while a poor correlation between Mo-EF and Cr-EF ($r^2 = 0.43$ not shown) indicates a more complex Cr control.

Fig. 8. Rare earth element and selected trace element distributions of Liblín detritic and pelagic sediments normalized to C1 chondrite (Boynnton, 1984) and PAAS (the post-Archean Australian Shale Composite; Taylor and McLennan, 1985).

Fig. 9. Variations in Mo vs. TOC, $\delta^{98}\text{Mo}$, S and Cr vs. $\delta^{53}\text{Cr}$, Al/Cr and Ce/Ce* values in detritic and pelagic sediments at Liblín. Note that error bars for $\delta^{53}\text{Cr}$ are smaller than symbol size.

Fig. 10. Photomicrographs of two types of pyrite in the black shales at Liblín with the mean trace element contents (in ppm). (a) Syngedimentary pyrite (Type I) represented by stratiform layers (composed of small pyrite crystals and framboids), that were folded most likely via slumping within not fully consolidated C_{org} - and S-rich rock matrix, (b) Recrystallized pyrite (Type II) represented by larger coarse-grained pyrite aggregates. Axio Imager A2m, Carl Zeiss, Reflected light image, A. Vymazalová.

Fig. 11. Mo-EF vs. U-EF variation diagram (adopted from Tribouillard et al., 2012) for the Liblín black shales. Note that Mo-EF and U-EF of the Liblín black shales are expressed to PAAS reference values in this figure.

Fig. 12. Fe_T/Al vs. S and $\delta^{56}\text{Fe}$ and $\delta^{56}\text{Fe}$ vs. S and Fe_2O_3 in clastic and pelagic sediments at Liblín.

Fig. 13. A schematic model of deposition of black shales at Liblín. The overall wedge compression and high-volume graywacke deposition via turbiditic currents (a) was interrupted by brief periods of co-seismic slip along the subduction zone megathrust, allowing

extension, basin subsidence, and deposition of black shales (b). The latter phase was also associated with extensive Si–Ba fluid percolation. Based on Normand et al. (2019).

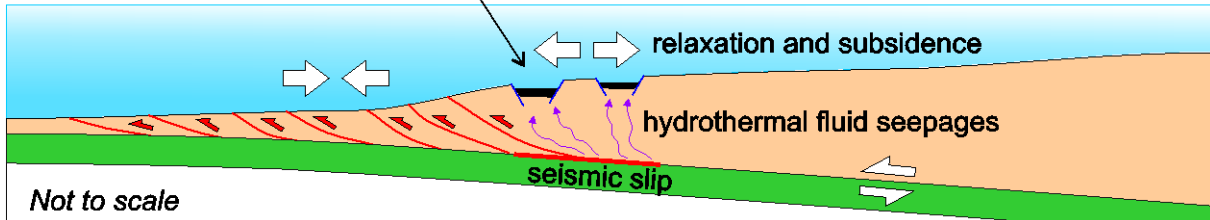
Journal Pre-proof

Declaration of interests

The authors declare that they have no known competing financial interests or personal relationships that could have appeared to influence the work reported in this paper.

The authors declare the following financial interests/personal relationships which may be considered as potential competing interests:

Journal Pre-proof

Early Cambrian (Blovic accretionary complex, Bohemian Massif)**Co-seismic period: accretionary wedge locally in extension, low sediment flux**Black shale deposition in small starved trench-slope basins:
low siliciclastic supply, Si-Ba fluid percolation

Journal Pre-proof

- Lower Cambrian black shales are present in the Blovice accretionary complex, Bohemian Massif
- Major redox proxies confirm black shale deposition under changing redox conditions
- Tectonic subsidence and varying supply of terrigenous arc-derived material were major control
- Early Cambrian $O_{2atm.}$ level of ~28 % was estimated based on Se/Co ratios in synsedimentary pyrite

Journal Pre-proof